Escola de Camins
Escola Tècnica Superior d'Enginyeria de Camins, Canals i Ports
UPC BARCELONATECH

Sinkhole development over karstic substratum. An MPM approach.

TREBALL FINAL DE MÀSTER

Treball realitzat per:
Lucía Belén Barandiarán Villegas

Dirigit per:
Dr. Eduardo Alonso Pérez de Ágreda
Dra. Núria Mercè Pinyol Puigmartí

Màster en:
Enginyeria del Terreny

Barcelona, **maig 2018**

Departament d'Enginyeria Civil i Ambiental

Abstract

Sinkholes are geohazards associated with karstic formations. Previous studies report that changes in water flow conditions, such as rainfall or water table decline, can trigger or accelerate this phenomenon because of material strength loss. The aim of this work is to carry out a numerical analysis using the Material Point Method (MPM) in order to study sinkhole developments over karstic substratum. The stability of a soil layer over a cavity is associated with soil arching effect. In order to analyze this phenomenon and evaluate the capabilities of method, a well-documented yielding trapdoor experiment is modelled with single-phase MPM. Then, a parametric study of the main variables related to the experiment is carried out. Finally, a simplified approach to study sinkhole developments in unsaturated soil with MPM modelling is presented. Results show that MPM is capable of modelling characteristic loading behaviour on the trapdoor throughout the experiment but presents difficulties in accurately assessing the soil arching mechanism. This limitation is mainly related to mesh dependency.

Acknowledgements

En primer lugar, quiero agradecer a mis asesores Eduardo Alonso y Núria Pinyol por brindarme la oportunidad de realizar mi Trabajo de Fin de Máster bajo su supervisión. Esta experiencia ha sido completamente enriquecedora tanto desde el plano académico como el personal.

Quiero extender un inmenso agradecimiento a Gaia di Carluccio, quien ha sido parte fundamental en el desarrollo de este trabajo. Sin su gran ayuda y disposición mi esfuerzo habría sido insuficiente.

A Alba Yerro le agradezco muchísimo haberme ayudado con mis primeros pasos en el MPM.

A Hanna, mi compañera, con especial cariño. Por todas las aventuras, el apoyo incondicional, lo que hemos aprendido juntas y porque me enseñó a creer en mí. A su hermana y madre también, Daniela y Aurora, que me han acogido como una más de la familia.

A mis amigas feministas radicales, que llegaron a acompañarme en el mejor momento de la vida.

To Neil and Chris, for providing me with the strength I sometimes needed.

Finalmente, a mi madre que nunca ha dudado en darme lo mejor que podía ofrecerme. Y a mi familia que siempre me acompaña desde la lejanía.

Table of Contents

List of Figures

List of Tables

1. Introduction

1.1. Sinkholes

Sinkholes are closed, circular depressions on soil or rock surface that constitute a frequent geohazard in karst, the characteristic landscape formed in soluble rock stratum (Waltham, 2008). Due to rock solubility, water flow creates caverns or large channels within the stratum that reach the surface or the cover layer, triggering sinkholes. Evaporite and carbonate rocks, like gypsum and calcite respectively, comprise karst formations. However, most research has been carried out in the latter in spite of evaporite's higher average dissolution rates (Gutiérrez et al, 2007).

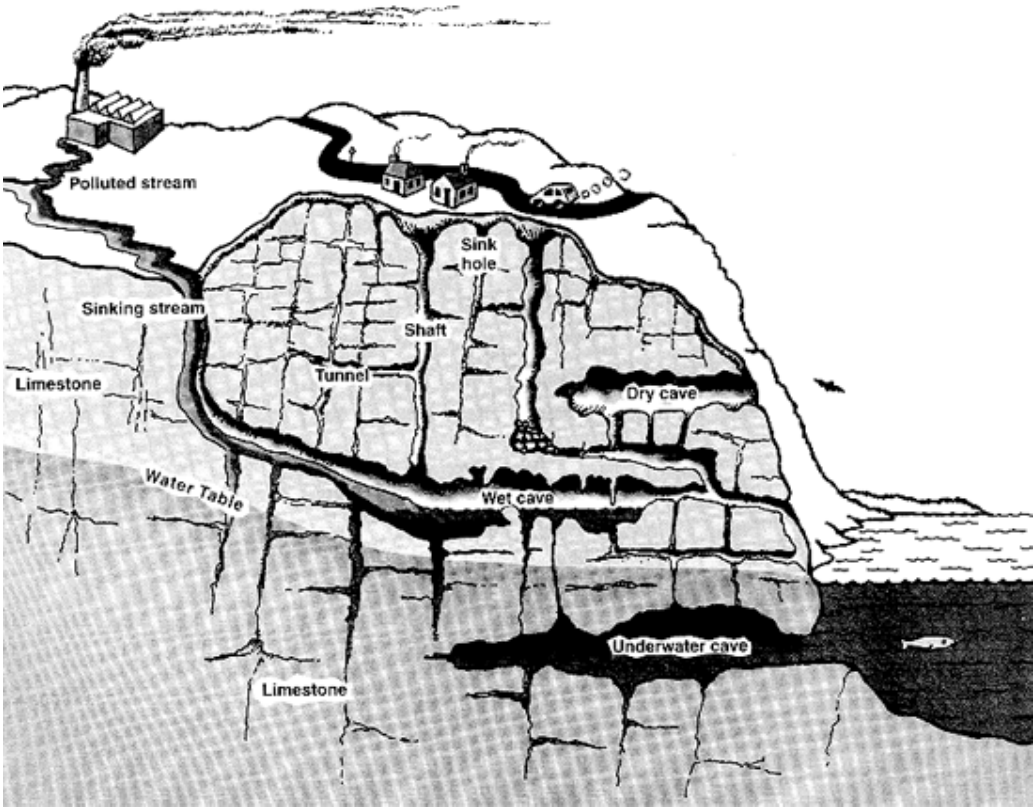

Figure 1.1 Scheme of karst formation. (U.S. Geological Survey Public Affairs Office, 2007)

Karst is found in different places around the world, yet, rainfalls and dense plant covers create optimum conditions for its development (Waltham et al, 2000). South Asia is a place widely known for its tower karst, as shown in Figure 1.2 and Figure 1.3 presents a *dolina*, Slovenic word for sinkhole.

Figure 1.2 Tower karst in China (Waltham, 2008)

Figure 1.3 *Dolina* in Slovenia. (Waltham, 2009).

Two main sinkhole categories are distinguished, solution and subsidence. The first group comprises depressions on the surface of karst rock exposed or barely covered karst whereas the second one involves deformation of a rock or soil layer over a karstic substratum. Gutiérrez et al (2008) proposed a genetic classification of subsidence sinkholes based on previous studies of evaporite karst in Spain by means of two terms, the material affected (cover, bedrock or caprock) and the main type of process involved (collapse, suffusion or sagging). Figure 1.4 shows schemes for every type of combination while Figures 1.5 and 1.6 present sinkholes in Saudi Arabia and England respectively.

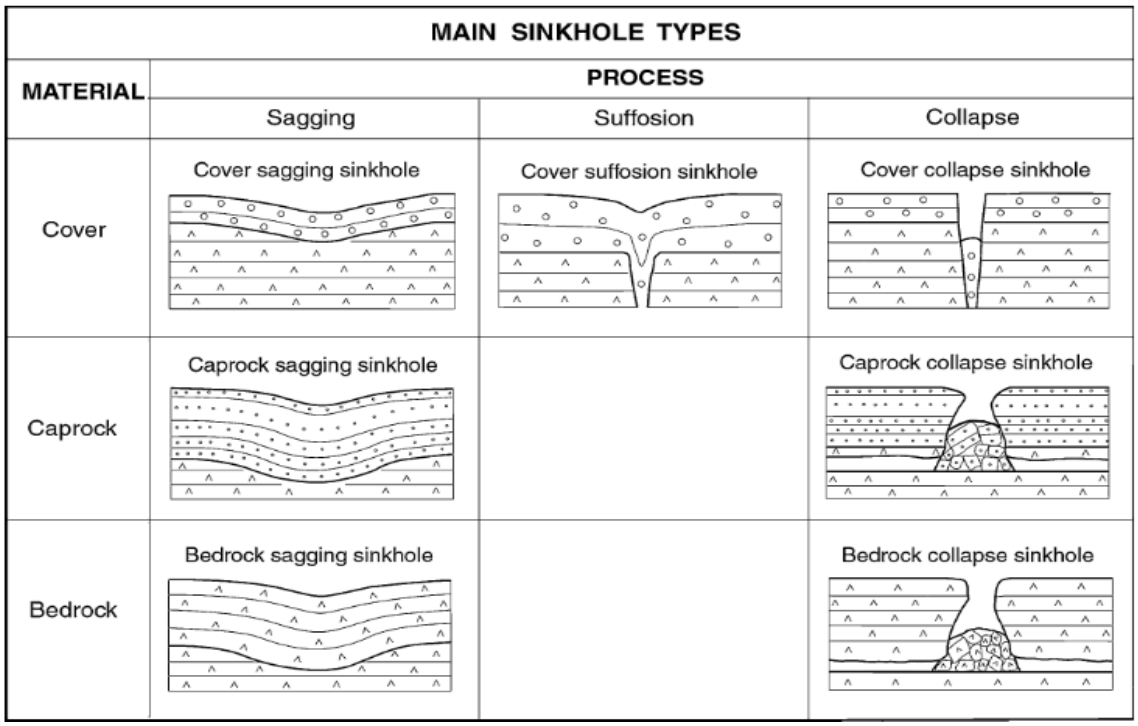

Figure 1.4 Main sinkhole types. (Gutiérrez et al, 2008).

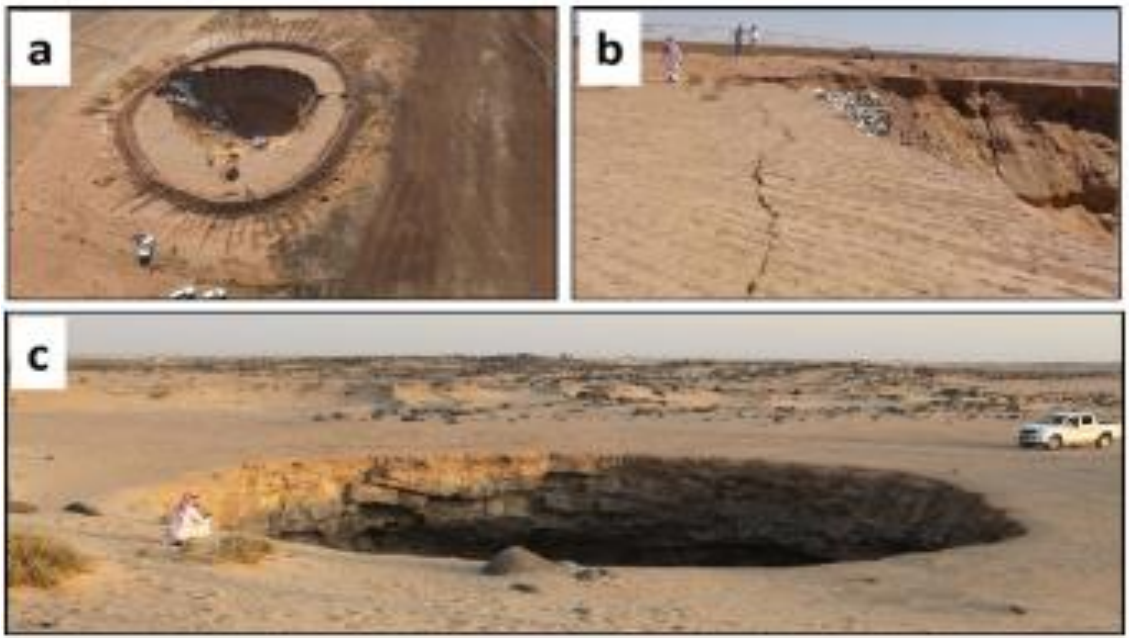

Figure 1.5 Cover collapse sinkholes in Saudi Arabia (Youssef et al, 2016).

Figure 1.6 Destructive sinkhole over gypsum stratum in a house in England (Waltham, 2009).

According to Gutiérrez et al (2007), changes in karst environment that may trigger or accelerate the development of sinkholes include:

Increased water input to the ground

- Its main effects are: favoring rock dissolution, increasing percolation that accelerates suffusion, increasing the weight of the sediments and the reduction of mechanical strength of the sediments. Rainfall events, floods, snow melting are natural processes that may trigger this water input, but also irrigation, leakages from pipes or canals, impoundment of water or runoff concentration due to urbanization or soak ways.

Water table decline

- Its main effects are: increasing the effective weight of the sediments (loss of buoyant support), generation of downward percolation favoring suffusion (especially if water table is lowered below rockhead) and reduction of mechanical strength by desiccation. Water table decline is triggered by sea level decline, entrenchment of drainage network, water abstraction or de-watering for mining operations and decline of water level in lakes.

Sinkhole development has been studied following several approaches, for instance a crack propagation and sloughing failure model was proposed (Tharp, 1999), numerical modelling of undrained collapse over a cavity using bound analysis in finite element methods (Augarde et al, 2003), experimental modelling in weakly cemented sands (Abdulla, 1996) and recent

studies include detection of sinkhole formation by strain profile measurements using fiber optics (Linker and Klar, 2015).

1.2. Scope of this work

The aim of this work is to carry out a numerical analysis using the Material Point Method in order to study sinkhole developments over karstic substratum by means of the following approach: given an unsaturated cohesive granular soil layer, a set of specific conditions, including geometry and strength parameters, will grant its stability over a (karstic) cavity without any type of support; however, a loss of strength caused by water inflow will produce collapse in soil, triggering a sinkhole.

In order to study the stability of the soil layer, soil arching effect is revised according to Iglesia et al (2014) approach. Given that yielding trapdoor experiments are used to study this effect, MPM code was used to model one of such experiments on a geotechnical centrifuge, carried out by Iglesia et al (2011). Finally, a simplified approach to study sinkhole developments in unsaturated soils using MPM is presented.

1.3. Outline and content

Chapter 1 presents a brief review on sinkholes, including classification, triggering factors and literature on the topic. The approach to study sinkhole developments followed in this work is also presented.

In Chapter 2 single-phase Material Point Method (MPM) formulation is presented according to Yerro (2015). Also, strain softening Mohr-Coulomb constitutive model (Yerro et al ,2014) is presented.

In Chapter 3, soil arching effect is presented according to Iglesia et al (2014) approach. In addition, a review on Iglesia et al (2011) yielding trapdoor experiments on a geotechnical centrifuge is presented.

Chapter 4 presents the characteristics of the model taking as reference one experiment carried out by Iglesia et al (2011). Main results are also presented and discussed.

In Chapter 5 a parametric study is carried out including normalized depth, mesh size and peak and residual friction angle.

Chapter 6 presents a simplified approach to study sinkhole developments in unsaturated soil using single-phase MPM code. Wang et al (2016) and Yerro et al (2014) have been taken as reference.

Chapter 7 and 8 present main conclusions and references respectively.

2. The Material Point Method

In the following sections, the Material Point Method (MPM) is studied, following Yerro (2015) presentation for the single-phase MPM formulation, including the governing differential equations, spatial and time discretization, solution algorithm, minimum time step criterion, boundary conditions and the strain softening Mohr-Coulomb constitute law.

2.1. Introduction

The solution of complex geotechnical problems demands the use of numerical methods and advanced techniques with the capacity of modelling several types of problems. Two main methods are identified according to the discretization approach: mesh-based and particle-based.

Mesh-based methods use a computational mesh to divide the continuum into a set elements and nodes. The algorithms of continuum mechanics take in account lagrangian or eulerian description of the motion. In the first one, the mesh follows the material and in the second one uses a fixed mesh and continuum moves with respect to the grid. Three classic types of mesh-based methods are the Finite Difference Method, the Finite Element Method and Finite Volume Method. Finite Element Method is the most used technique in geotechnics for finding approximate solutions to boundary value problems (Zienkiewicz, 1967). One disadvantage is the difficulty to model large deformations.

Particle methods or meshless methods were developed as a means of avoiding the difficulties of mesh-based methods. They are based on free particles without relationships between one to another and move attached with the domain, following lagrangian description. Both discrete and continuum domains can be modelled. For instance, Discrete Element Method (DEM) and Smoothed Particle Hydrodynamics (SPH) consist of two types of particle methods. Disadvantages include contact properties between particles and the application of boundary conditions respectively. Figure 2.1 Presents a scheme of both methods.

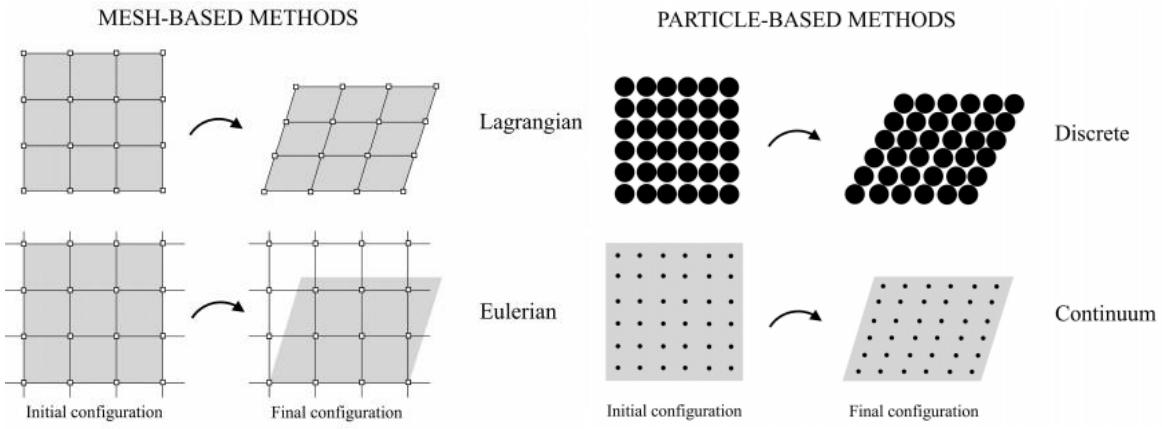

Figure 2.1 Scheme of mesh-based and particle-based methods. (Yerro, 2015).

MPM was initially developed for modelling fluid flow by Harlow et al (1964) in Los Alamos National Laboratory and was named Particle-In-Cell (PIC) method. Sulsky and Schreyer (Sulsky et al, 1994; Sulsky and Schreyer, 1996; Sulsky et al, 1995) extended its approach for solid mechanics modelling.

MPM is considered a mixed method, between particle-based methods and Finite Element Method (FEM) since it assumes the media in two different frames. The continuum is divided in material points that represent a subdomain and its mass, which is fixed during the entire calculation to ensure mass conservation. Material points store and carry other information such as velocities, strains and stresses, and move attached with deformations of the body. This consists of a lagrangian description of the media. A computational mesh covers the full domain of the problem and the discrete governing equations are solved in the associated nodes. Material points transfer the information required to solve the equations at every time step by means of mapping functions, which can be the same as the ones employed in FEM. Boundary conditions can be applied both at material points and nodes. Material point information is updated from mesh, also using mapping functions. Data from the mesh is discarded and reset to the original configuration every step. Figure 2.2 presents the space discretization for MPM.

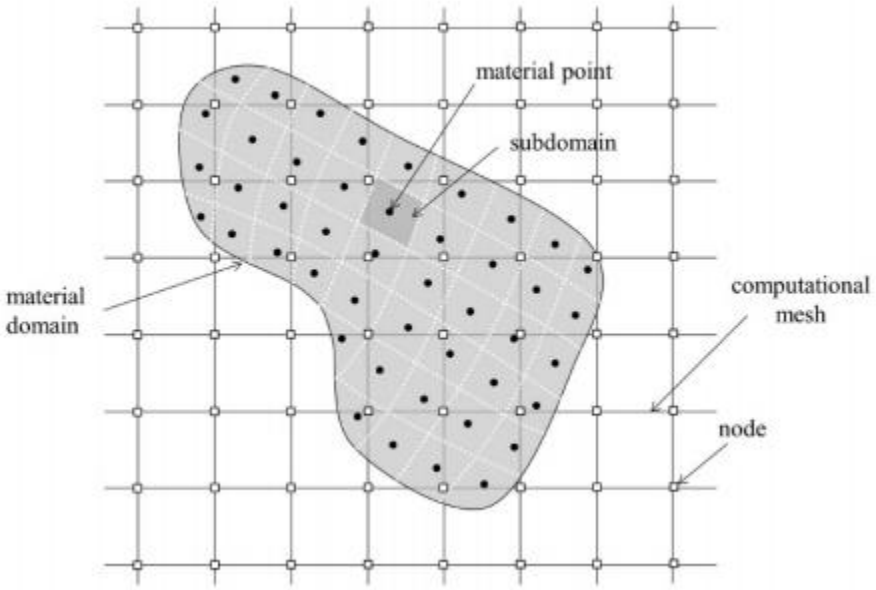

Figure 2.2 Space discretization for Material Point Method (Yerro, 2015).

2.2. Governing Equations

A given part of the continuum spans over a volume $\boldsymbol{\Omega_0}$ at an arbitrary initial time t_0, and for any instant of time t, over a volume $\boldsymbol{\Omega_\tau}$. Material points for last configuration are defined by the coordinate vector $\mathbf{X}$ and position vector $\mathbf{x} = \varphi(\mathbf{X}, \mathrm{t})$. Displacement vector is defined by $\mathbf{u}(\mathbf{x}, \mathrm{t}) = \mathbf{x}(\mathrm{t}) - \mathbf{x}(t_0)$, velocity vector by $\mathbf{v}(\mathbf{x}, \mathrm{t})$ and mass density by $\boldsymbol{\rho}(\mathbf{x}, \mathrm{t})$. Also, Cauchy stress tensor is defined by $\boldsymbol{\sigma}(\mathbf{x}, \mathrm{t})$.

Mass conservation is determined by the following expression

$$\dot{\rho} + \rho \nabla \cdot \mathbf{v} = 0 \qquad \text{(Eq. 2.1)}$$

Momentum balance equation can be written as

$$\rho \mathbf{a} = \nabla \cdot \boldsymbol{\sigma} + \rho \mathbf{b} \qquad \text{(Eq. 2.2)}$$

Where **a** stands for acceleration and **b** for body force vector.

Prescribed traction and prescribed displacements are boundary conditions defined as follows

$$\boldsymbol{\sigma}(\mathbf{x}, \mathrm{t}) \cdot \mathbf{n} = \hat{\mathbf{t}}(t) \qquad \text{(Eq. 2.3)}$$
$$\mathbf{u}(\mathbf{x}, \mathrm{t}) = \hat{\mathbf{u}}(t) \qquad \text{(Eq. 2.4)}$$

Where **n** is the outward unit normal vector of the free surface, $\hat{\mathbf{t}}(t)$ the surface traction vector and $\hat{\mathbf{u}}(t)$ the displacement vector. Equations 2.3 and 2.4 are applied in $\partial\Omega^t$ and $\partial\Omega^u$ respectively.

The constitutive equation defined by stress and strain rate vectors is,

$$\dot{\boldsymbol{\sigma}} = \dot{\mathbf{D}} \cdot \dot{\varepsilon} \qquad \text{(Eq. 2.5)}$$

2.3. Discretization of Governing Equations

Continuum is discretized by means of elements, which contain a fixed value of mass in time. In this case, MPM uses a determined number of material points N_p, and assigns each one a mass m_p where p=1, 2, …, N_p. The density equals the total mass of the group as following

$$\rho(\mathbf{x}, \mathrm{t}) = \sum_{p=1}^{N_p} m_p \delta(\mathbf{x} - \mathbf{x}_p) \qquad \text{(Eq. 2.6)}$$

Where $\delta(\mathbf{x})$ is the Dirac delta function. Since MPM uses the same computational mesh as FEM, composed by nodes and elements, standard nodal shape functions N_j relate the position of any point in the domain with the nodes. According to this, displacement of a material point can be calculated with the expression,

$$\mathbf{u}_p\left(\mathbf{x}_p, t\right) = \sum_{j=1}^{N_n} \mathbf{u}_j(t) N_j(\mathbf{x}_p, t) \qquad \text{(Eq. 2.7)}$$

Where N_n is the number of nodes, and the same formula is used for velocity and acceleration.

The weak form of momentum balance equation can be obtained by Weighted Residuals method,

$$\int_{\Omega} \delta\mathbf{u} \cdot \rho\mathbf{a} d\Omega = \int_{\delta\Omega^t} \delta\mathbf{u} \cdot \hat{\mathbf{t}} d\Omega^t - \int_{\Omega} \nabla\delta\mathbf{u} : \boldsymbol{\sigma} d\Omega + \int_{\Omega} \delta\mathbf{u} \cdot \rho\mathbf{b} d\Omega \qquad \text{(Eq. 2.8)}$$

Where $\delta\mathbf{u}$ is a test function and its value is zero for prescribed displacement.

By combining spatial discretization formulas and the constitutive equation, the weak form can be transformed in the following expression:

$$\sum_{j=1}^{N_n}\left(\sum_{p=1}^{N_p} m_p N_i^p N_j^p\right)\mathbf{a_j} = \int_{\delta\Omega^t} N_i^p \hat{\mathbf{t}} d\partial\Omega^t - \sum_{p=1}^{N_p} \mathbf{B_i^p} \cdot \boldsymbol{\sigma_p} V_p + \sum_{p=1}^{N_p} m_p N_i^p \mathbf{b} \qquad \text{(Eq. 2.9)}$$

Where V_p represents the volume a material point, $N_i^p = N_i^p(\mathbf{x}_p, t)$, and $\mathbf{B_i^p}$ corresponds with the nodal matrix for a given point. This matrix consists of the nodal shape spatial derivatives.

The discretized form yields

$$\mathbf{M} \cdot \mathbf{a} = \mathbf{F}^{ext} - \mathbf{F}^{int} \qquad \text{(Eq. 2.10)}$$

With

$$\mathbf{M} = \left(\sum_{p=1}^{N_p} m_p \mathbf{N}^{p^T} \cdot \mathbf{N}^p\right) \qquad \text{(Eq. 2.11)}$$

$$\mathbf{F}^{int} = \sum_{p=1}^{N_p} \mathbf{B_i^p} \cdot \boldsymbol{\sigma_p} V_p \qquad \text{(Eq. 2.12)}$$

$$\mathbf{F}^{ext} = \int_{\partial\Omega} N_i^p \hat{\mathbf{t}} d\partial\Omega^t + \sum_{p=1}^{N_p} m_p N_i^p \mathbf{b} \qquad \text{(Eq. 2.13)}$$

To simplify computations, a lumped matrix can be calculated. Instead of using the matrix provided by Equation 2.11, the lumped matrix can be employed. It is a diagonal matrix where m_i is calculated by the sum of the components of every row in the consistent matrix. Brackbill et al (1988) found that some dissipation of kinetic energy as a result of this change. Replacing $\sum_{j=1}^{N_n} N_j^p = 1$

$$\mathbf{M}^L = \sum_{p=1}^{N_p} m_p \mathbf{N}^p \qquad \text{(Eq. 2.14)}$$

Then the subscript L is removed and the mass matrix becomes the lumped matrix. Strain increment at material point is calculated with nodal velocity gradients, following

$$m_i \mathbf{v}_i = \sum_{p=1}^{N_p} m_p N_i^p \mathbf{v}_p \qquad \text{(Eq. 2.15)}$$

And velocities are calculated with

$$\mathbf{v}_i = \frac{1}{m_i}\sum_{p=1}^{N_p} m_p N_i^p \mathbf{v}_p \qquad \text{(Eq. 2.16)}$$

2.4. Time Discretization

For a given *k* time step, the Equation can be rewritten as

$$\mathbf{M}^{\boldsymbol{k}} \cdot \mathbf{a}^{\boldsymbol{k}} = \mathbf{F}^{ext^k} + \mathbf{F}^{int^k} \qquad \text{(Eq. 2.17)}$$

Euler explicit time integration scheme is used to estimate the velocities in time. It is used to solve ordinary differential equations with a given initial value. If $\mathbf{v}^k$ is the velocity at time t^k, the velocity at following time step t^{k+1} is

$$\mathbf{v}^{k+1} = \mathbf{v}^k + \Delta t \mathbf{a}^k \qquad \text{(Eq. 2.18)}$$

Displacements at time t^{k+1} are estimated using the updated velocity $\mathbf{v}^{k+1}$

$$\mathbf{u}^{k+1} = \mathbf{u}^k + \Delta t \mathbf{v}^k \qquad \text{(Eq. 2.19)}$$

2.5. Solution Algorithm

Initialization of material points includes initial conditions, material parameters and constitutive variables. Information about housekeeping is also included, for instance the element each particle initially belongs to and the initial number of particles per element.

The algorithm presented is a summary of the solution procedure, as presented by Yerro (2015).

I. The nodal mass is calculated using shape functions and the lumped matrix at time t^k is generated (Equation 2.14).

II. The internal and external forces are calculated in the nodes with Equations 2.12 and 2.13.

III. The nodal accelerations $\mathbf{a}_i^k$ are determined with momentum balance equation (2.17)

IV. The velocity at material points is updated with Equation 2.18 with the form

$$\mathbf{v}_p^{k+1} = \mathbf{v}_p^k + \Delta t \sum_{j=1}^{N_n} m_p N_i^{p\,k} \mathbf{a}_j{}^k \qquad \text{(Eq. 2.20)}$$

V. The updated nodal velocity is calculated with Equation 2.16 with the form

$$\mathbf{v}_j^{k+1} = \frac{1}{m_j{}^k}\sum_{p=1}^{N_p} m_p N_j^{p\,k} \mathbf{v}_p{}^{k+1} \qquad \text{(Eq. 2.21)}$$

VI. Particle positions are updated taking Equation 2.19 with the form

$$\mathbf{x}_p^{k+1} = \mathbf{x}_p^k + \Delta t \sum_{j=1}^{N_n} N_j^{pk} \mathbf{v}_j{}^{k+1} \qquad \text{(Eq. 2.22)}$$

VII. The increment strain of material points can be expressed in function of the nodal velocity following,

$$\Delta\varepsilon_p^{k+1} = (\sum_{j=1}^{N_n} \mathbf{B}_j^{pk} \mathbf{v}_j{}^{k+1})\Delta t \qquad \text{(Eq. 2.23)}$$

VIII. Stresses are calculated with a material constitutive model as Equation 2.5.

IX. Material properties such as volume and density are updated considering the increment of volumetric strain.

X. Nodal values are discarded and material points carry the updated information. The computational grid is reset.

2.6. Minimum Time Step Criterion

Given that Euler explicit time integration is conditionally stable, the Courant-Friedrichs-Levy condition is applied to obtain the critical time interval required to achieve a stable solution throughout the calculation according to

$$\Delta t_{crit} = \frac{L_{min}}{c} \qquad \text{(Eq. 2.24)}$$

and

$$c = \sqrt{\frac{E_c}{\rho}} \qquad \text{(Eq. 2.25)}$$

Where E_c is the constrained modulus of solid media and L_{min} is the minimum size of the element, for instance in tetrahedra elements this corresponds with the minimum height. In order to be more conservative, a reducing factor is applied to the critic time step, as following:

$$\Delta t = \alpha_C \Delta t_{crit} \qquad \text{(Eq. 2.26)}$$

2.7. Boundary Conditions

In order to solve mechanical problems, two types of boundary conditions are applied: essential and natural. Essential condition consists of prescribed solid velocity whereas natural condition consists of prescribed traction. The second one is applied directly in the solution reducing degrees of freedom and the second one in a secondary variable, in this case in the weak form of governing equations.

Boundary conditions are applied at the nodes because motion equations are solved in said elements. However, moving boundary conditions present a problem because it needs to be attached to the nodes throughout the body movement. Given that in standard MPM

formulation the mesh remains constant, this condition is carried by the material points. For natural conditions this leads to some inaccuracies, because this condition has to be distributed from the material point to the nodes and the element takes part of the contour. Therefore, the contour thickness corresponds with the size of the element and the boundary condition affects every material point within the cell. A form to reduce this error is to employ a fine mesh.

Another problem arises when a force does not present a prescribed direction. This means that when the body moves, the direction needs to be recalculated in material points, leading to more computational cost. Figure 2.3 (a) shows a beam with zero prescribed velocity and (b) the same beam with a natural boundary condition.

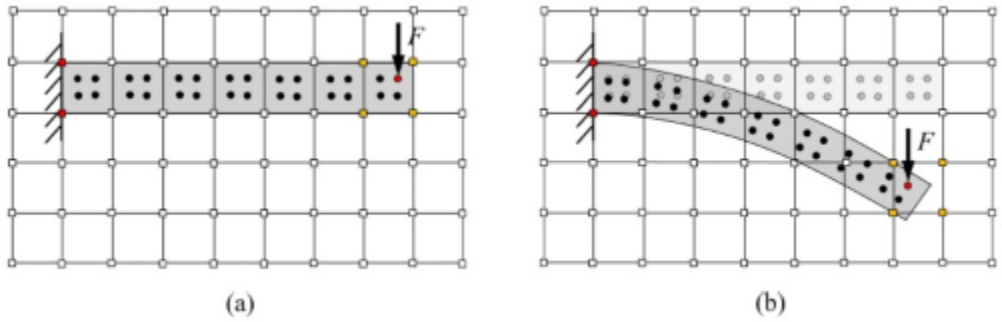

Figure 2.3 (a) Beam with prescribed velocity of zero. (b) Beam with natural moving boundary condition. (Yerro, 2015)

Additionally, several problems in geotechnical engineering involve boundary limits that are not clearly defined, for instance footings, as the scheme is Figure 2.4 shows. Considering that MPM is a dynamic formulation code, applied loads trigger waves that are reflected in the boundaries, whereas in real case they are spread out in the ground. This reflection affects the solution.

One form to avoid this effect is setting the boundaries far enough, though computational time required will increase. Lysmer and Kuhlmeyer (1969) proposed the use of contours on dampers considering a viscous force in boundary nodes. Al-Kafaji (2013) adapted this concept to MPM by means of Kelvin-Voigt elements, which take in account the combination in parallel of a spring and a dashpot, as shown in Figure 2.4, that represent a virtual layer with the capacity of absorbing wave reflections. This force has to be included in the dynamic momentum balance.

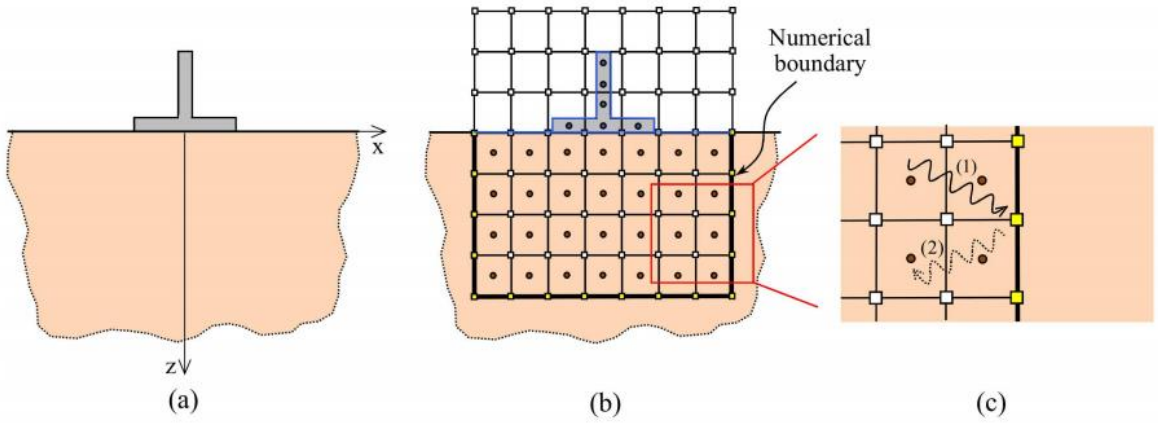

Figure 2.4 (a) Scheme for shallow footing. (b) Distribution of material points and mesh. (c) Reflected wave. (Yerro, 2015)

2.7.1. Zero Kinematic Boundary Condition

These conditions are applied in the same form as in LagrangianFEM and are simple to introduce in MPM formulation. This condition is used to set zero prescribed kinetic boundary conditions for a node that becomes active. Figure 2.5 presents an example. Zero traction is automatically satisfied.

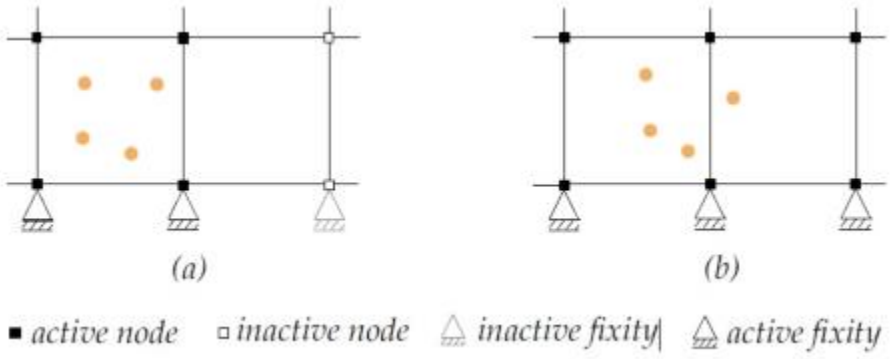

Figure 2.5 Kinematic boundary conditions for active and inactive nodes. (a) Inactive fixity. (b) Active fixity. (Al-Kafaji, 2013)

2.7.2. Traction Boundary Conditions

Boundary material points are material points located next to the element border and external forces applied at traction boundary are mapped to said points. They carry the external forces information throughout the calculation. Figure 2.6 shows a scheme of this case. Equation 2.27 calculates the traction at boundary material point as follows

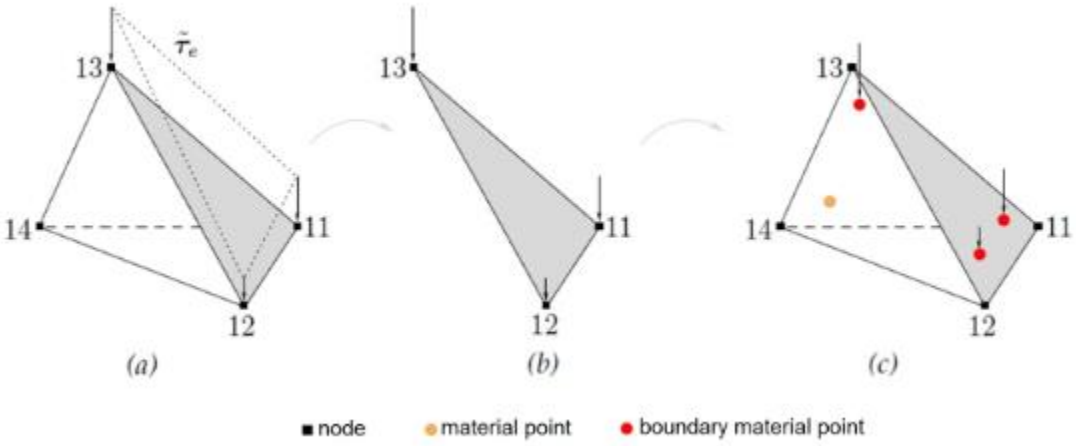

Figure 2.6 Traction mapped from boundary material point to nodes of the element. (Al-Kafaji, 2013)

$$\tau_e(\mathbf{x}_{\mathrm{MP}}) \approx \sum_{i=1}^{n_{tri}} \mathrm{N}_i(\xi_{\mathrm{MP}})\, \tau_e(\mathbf{x}_{\mathrm{i}}) \qquad \text{(Eq. 2.27)}$$

Where τ_e is the traction vector applied at the triangular surface, N_i is the shape function of node i on the triangular surface element, ξ_{MP} correspond with the coordinates of material point in the triangular element, which represent the projection of this point on the triangular surface.

The traction force vector is calculated as

$$\mathbf{f}_{MP}^{trac} = \tau_e(\mathbf{x}_{\mathrm{MP}}) \frac{\mathrm{S_e}}{\mathrm{n_{ebMP}}} = \frac{\mathrm{S_e}}{\mathrm{n_{ebMP}}} \sum_{i=1}^{n_{tri}} \mathrm{N}_i(\xi_{\mathrm{MP}})\, \tau_e(\mathbf{x}_{\mathrm{i}}) \qquad \text{(Eq. 2.28)}$$

Where $\mathrm{n_{ebMP}}$ corresponds with the number of material points located next to loaded surface and $\mathrm{S_e}$ is the area of the triangular loaded surface. The direction and magnitude of the vector is kept throughout the calculation. As the body moves, the tractions are mapped from the boundary material points to the element nodes, according to the following expression

$$f^{trac} = \sum_{\mathrm{el}=1}^{\mathrm{no_{el}}} \sum_{\mathrm{MP}=1}^{\mathrm{no_{MP,el}}} \mathbf{N}^{\mathrm{T}}(\xi_{\mathrm{MP}})\, \mathbf{f}_{MP}^{trac} \qquad \text{(Eq. 2.29)}$$

As mentioned before in this section, force is distributed to the materials points in the elements at the border of the boundary, and a form to reduce the error associated is to assign a small thickness of elements along the boundary.

2.8. Strain Softening Constitutive Model

The strain softening Mohr-Coulomb law was introduced in Yerro et al (2014) in order to model strength loss that is triggered after peak strength conditions.

The Mohr-Coulomb yield surface can be written as

$$q = c' \cos\varphi' + p' \sin\varphi' \qquad \text{(Eq. 2.30)}$$

Where p' and q represent the effective volumetric and deviatoric stresses,

$$q = \frac{\sigma_1' - \sigma_3'}{2} \qquad \text{(Eq. 2.31)}$$

$$p' = \frac{\sigma_1' + \sigma_3'}{2} \qquad \text{(Eq. 2.32)}$$

Where σ_1' and σ_3' are the maximum and minimum effective principal stresses.

The softening behaviour is applied by reducing the effective strength parameters (φ' and c') with the accumulated equivalent plastic strain ε_{eq}^p according to the following exponential softening rules:

$$c' = c'_r + (c'_p - c'_r)e^{-\eta\varepsilon_{eq}^p} \qquad \text{(Eq. 2.33)}$$

$$\varphi' = \varphi'_r + (\varphi'_p - \varphi'_r)e^{-\eta\varepsilon_{eq}^p} \qquad \text{(Eq. 2.34)}$$

The deviatoric plastic strain invariant is defined as

$$\varepsilon_{eq}^p = \sqrt{\frac{2}{3}\mathbf{e}^p : \mathbf{e}^p} \qquad \text{(Eq. 2.35)}$$

The model requires the specification of peak (c'_p, φ'_p) and residual (c'_r, φ'_r) strengths. Also, a calibration parameter η is necessary to control the rate of strength decrease. Figure 2.7 presents the influence of η in a simple shear test simulation, where the brittle soil is modelled by a row of elements. A vertical stress of 50kPa was applied to a rigid layer above the soil layer with a confining horizontal stress of 25 kPa.

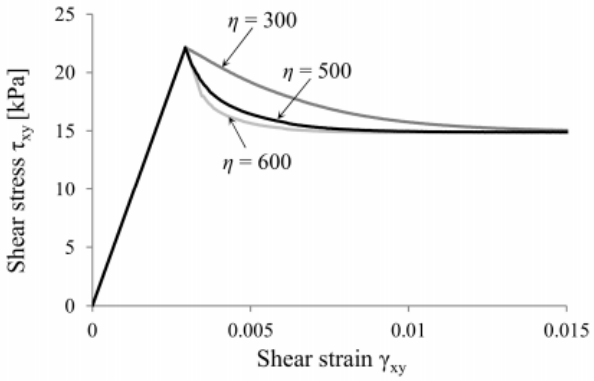

Figure 2.7 Influence of η in the evolution of shear stress (Yerro, 2015)

3. The Trapdoor Experiment

In this chapter, the trapdoor experiment and the theory behind soil arching is introduced. Iglesia et al (2014) study on soil arching with centrifuge tests and its main conclusions are presented.

3.1. Introduction

Underground structures such as anchors, tunnels, or plates present different stiffness from the surrounding soil, which leads to local stress redistribution and ultimately to settlements on ground surface. If the stiffness of the material is lower than that of the soil, active arching will develop by means of a load decrease over the inclusion with a load increase of adjacent soil. Conversely, if the stiffness is higher, load over the inclusion will increase and passive arching will take place. Yielding trapdoor experiments were first performed by Engesser (1882) in order to assess soil arching effect on sands, and later by Terzaghi (1936), Ladanyi and Hoyaux (1969), Vardoulakis et al (1981), Evans (1983), Stone (1998), Adachi et al (1997), Dewoolkar et al (2007), Chevalier et al (2009) and Costa et al (2009). Figure 3.1 shows a scheme of an active trapdoor experiment. According to previous investigation, the arching mechanism mainly depends on soil friction angle φ, the soil layer depth to trapdoor length H/B ratio and the displacement of the yielding trapdoor δ.

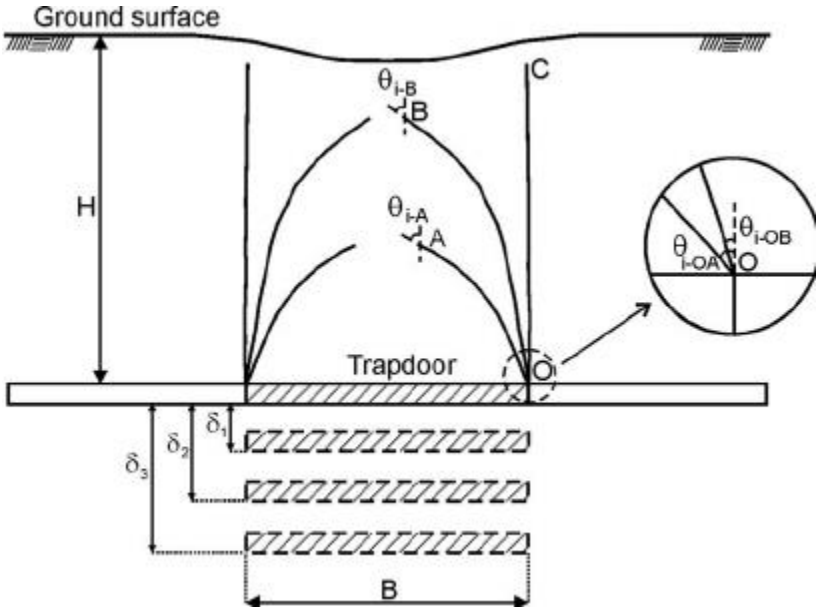

Figure 3.1 Active trapdoor experiment scheme. (Costa et al, 2009)

3.2. Soil Arching Effect Theory

The theory explained in this section is based on Iglesia et al (2014) study on soil arching. It consists of a “physical arch”, following Engesser (1882) approach, developed over the

trapdoor, which would be compatible with the negligible settlements reported on the surface of the soil layers used in the such experiments with a geotechnical centrifuge.

Once the trapdoor begins to descend, a slip surface with the shape of a half parabola is formed right above the trapdoor. The tangent angle of the curve with respect to a vertical plane at the edge of the trapdoor is assumed to be the dilatancy angle ψ, that according to an associated flow rule, corresponds with the friction angle φ. Because of trapdoor displacement, the former geostatic equilibrium in no longer possible and therefore the stresses redistribute in the soil to the sides of the parabola, leading to an increase in the lateral stresses σ_{hr} at its bottom. The total reaction force V in the trapdoor takes in account both the weight of the soil W below the slip surface and the vertical stress σ_{vr} triggered by the lateral stress σ_{hr}. Figure 3.2 presents the slip surface and the loads on the trapdoor.

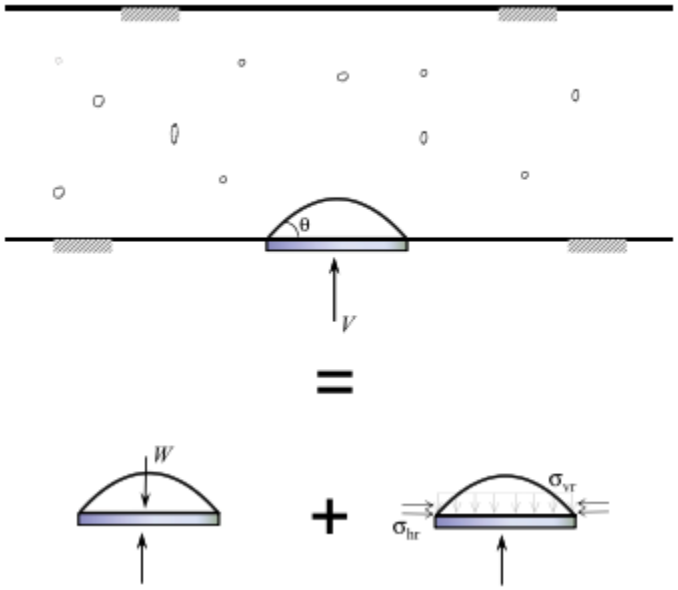

Figure 3.2 Slip surface and loads on the trapdoor (Iglesia et al, 2014).

The weight W of soil per unit of width can be calculated by,

$$W = \frac{\gamma B^2 \tan(\theta)}{6} = \frac{\gamma B^2 \tan(90°-\varphi)}{6} = \frac{\gamma B^2 \cot\varphi}{6} \qquad \text{(Eq. 3.1)}$$

While the vertical stress σ_{vr} can be estimated following the Engesser's (1882) approach, using a loaded imaginary structural arch of dh width. Figure 3.3 presents a scheme of this analysis, where the arch has the same shape as the parabola, σ_{hr} is constant at the bottom of the entire arch and equals dF_h divided by dh.

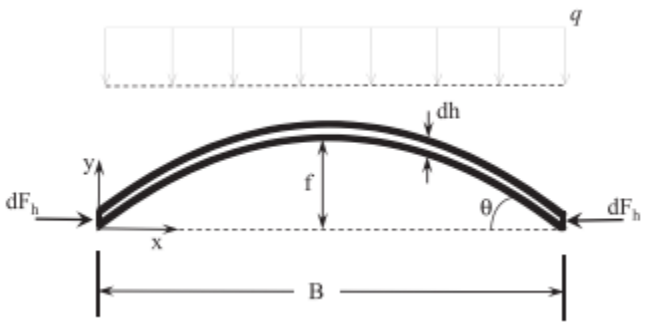

Figure 3.3 Imaginary structural arch. (Iglesia et al, 2014)

The arch also represents a failure surface and then it is possible to calculate a Mohr stress diagram at the edge of the trapdoor (Figure 3.4),

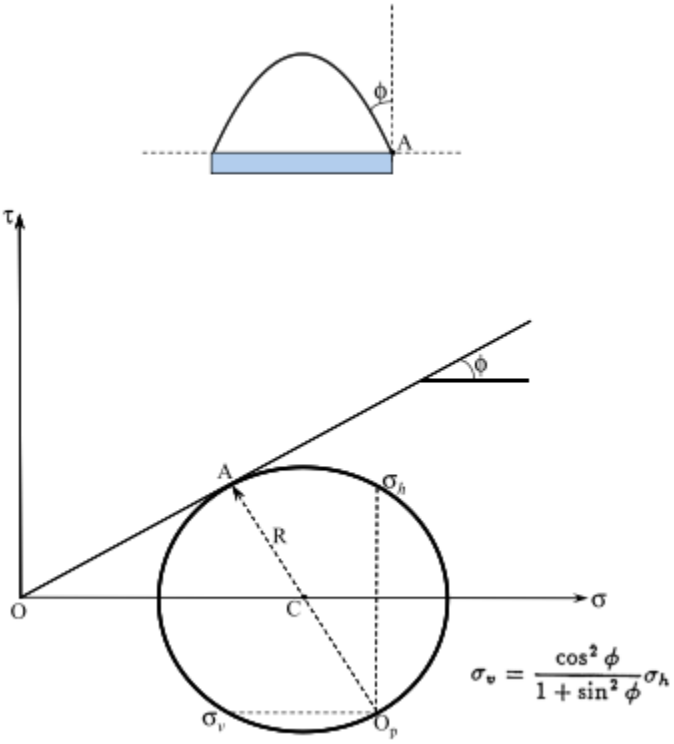

Figure 3.4 Mohr diagram for stress state at the edge of the trapdoor. (Iglesia et al, 2014)

Which yields the following expression,

$$\sigma_{vr} = K_E \sigma_{hr} \qquad \text{(Eq. 3.2)}$$

and,

$$K_E = \frac{\cos^2 \varphi}{1+\sin^2 \varphi} \qquad \text{(Eq. 3.3)}$$

In order to calculate σ_{vr}, the lateral stress σ_{hr} has to be estimated. As the trapdoor load decreases from the initial geostatic value, the difference between them is redistributed to the sides. The structural arch works as a means of quantifying the lateral thrust $dF_h = \sigma_{vr}/dh$ when subjected to this load state (γH - σ_{vr}). According to Engesser (1882) approach, the uniform load q over the arch relates to such difference and equals the imaginary arch weight:

$$q = dh\left(\gamma - \frac{\sigma_{vr}}{H}\right) \qquad \text{(Eq. 3.4)}$$

The relation between the lateral thrust dF_h and the load q is,

$$dF_h = \frac{qB^2}{8f} = \frac{qB}{2\tan\theta} = \frac{qB}{2\cot\varphi} \qquad \text{(Eq. 3.5)}$$

Where the rise of the arch f is $(B\tan\theta)/4$. Dividing the former expression by dh and replacing q,

$$\sigma_{hr} = \frac{dF_h}{dh} = \frac{B}{2\cot\varphi}\left(\gamma - \frac{\sigma_{vr}}{H}\right) \qquad \text{(Eq. 3.6)}$$

Substituting σ_{hr} for σ_{vr} following K_E formula,

$$\sigma_{vr} = \frac{HB\gamma K_E}{2H\cot\varphi + BK_E} \qquad \text{(Eq. 3.7)}$$

The reaction force V in the trapdoor takes in account the weight W and the effect of σ_{vr},

$$V = \gamma B^2\left(\frac{HK_E}{2H\cot\varphi + BK_E} + \frac{\cot\varphi}{6}\right) \qquad \text{(Eq. 3.8)}$$

And the average stress in the trapdoor is,

$$p_m = \gamma B\left(\frac{HK_E}{2H\cot\varphi + BK_E} + \frac{\cot\varphi}{6}\right) \qquad \text{(Eq. 3.9)}$$

Finally, normalizing the former expression with the geostatic stress $p_o = \gamma H$ yields the active load ratio,

$$\frac{p_m}{p_0} = \frac{B}{H}\left(\frac{K_E}{2\cot\varphi + \frac{B}{H}K_E} + \frac{\cot\varphi}{6}\right) \qquad \text{(Eq. 3.10)}$$

Following Iglesia et al (2014) approach, a similar expression is proposed for a triangular shaped soil arch,

$$\frac{p}{p_0} = \frac{B}{H}\left(\frac{K_E}{4\cot\varphi + \frac{B}{H}K_E} + \frac{\cot\varphi}{4}\right) \qquad \text{(Eq. 3.11)}$$

Where the rise of the arch *f* is $(B\tan\theta)/2$. According to their investigation results, this type of arch could develop after the parabolic arch.

If the trapdoor further displaces, vertical slip surfaces will develop from the edges of the trapdoor, consequently the parabola or triangle shaped arch will no longer be sustained and load over the trapdoor will increase. The ultimate state of arching consists of a prism of soil with fully mobilized shear strength at the sides, and the formula for its active load ratio is,

$$\frac{p}{p_0} = \frac{B}{2HK\tan\varphi}\left[1 - e^{-2K\tan\varphi(H/B)}\right] \qquad \text{(Eq. 3.12)}$$

According to Iglesia et al (2014), the common value used for *K* is K_a, active lateral earth pressure coefficient, though it assumes zero shear stress at the sides. They state that the most theorically sound value of *K* is given by Krynine (1945) whose formula is the same as K_E, except that for the ultimate state at larger displacements, $\sigma_{vr} > \sigma_{hr}$ whereas for initial arching $\sigma_{hr} > \sigma_{vr}$. A formula for an intermediate state is also proposed, assuming that the height of full shear strength mobilized is the rise of the triangular arch, $(B\tan\theta)/2$,

$$\frac{p}{p_0} = \frac{B}{2HK\tan\varphi}\left[1 - e^{-K}\right] \qquad \text{(Eq. 3.13)}$$

In Figure 5 a scheme of triangular shaped and terminal state arch is presented:

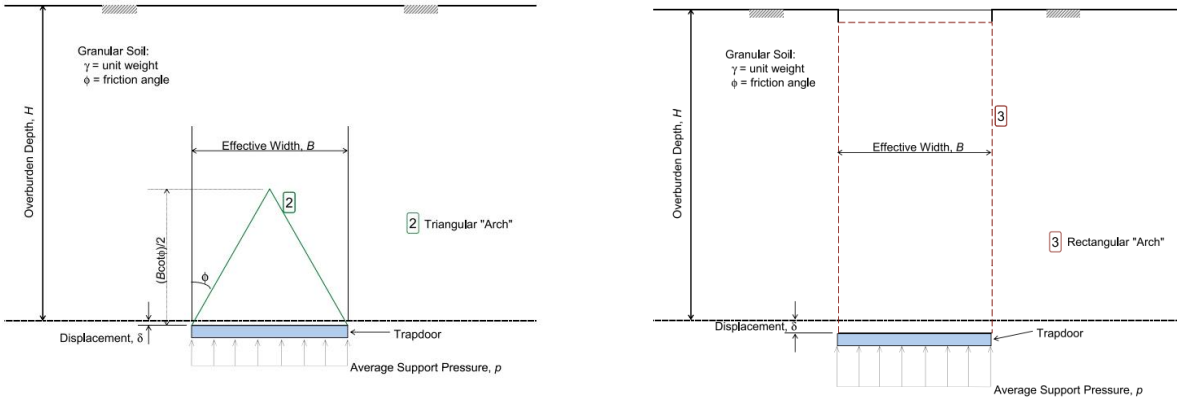

Figure 3.5 Triangular shaped and terminal state arch. (Iglesia et al 2014)

3.3. Investigation of Soil Arching with Centrifuge Tests (Iglesia et al, 2014)

Iglesia et al (2011) presented a study for the validation of a centrifuge test via trapdoor experiments in sand and glass beads and its results were later analyzed in light of soil arching investigation in 2014.

3.3.1. Model Setup

The model consists of a soil containing box, named strongbox, made from aluminum and a motorized device that activates the trapdoor movement. The strongbox aluminum plates are 12.7 mm thick and its dimensions are 406 mm long, 330 mm wide and 254 mm high. The bottom platform is composed by a 12.7 mm-thick aluminum plate over of a 50.8 mm-thick lexan (thermoplastic polycarbonate resin) pieces adjacent to the trapdoor sides. Three sets of trapdoor width were used: 12.7, 25.4 and 50.8 mm, and spacers were employed to fit them.

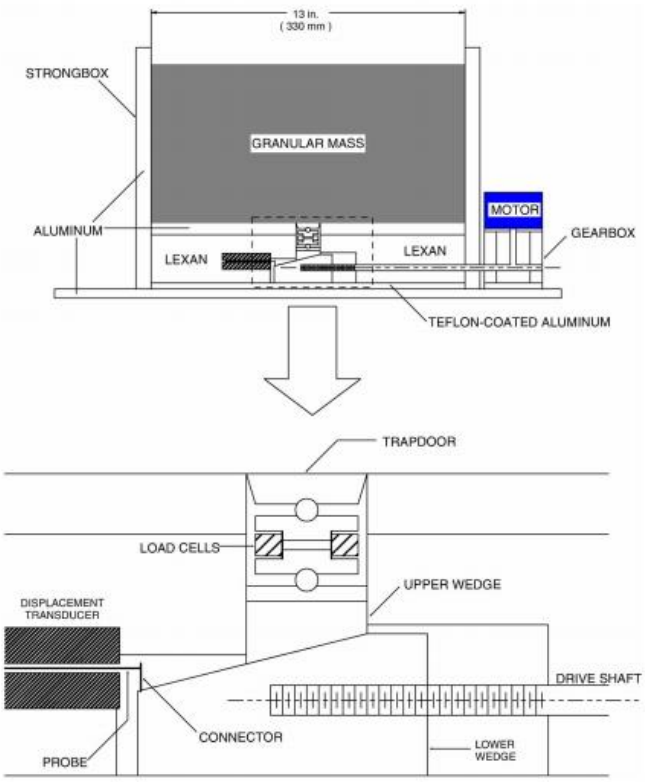

Figure 3.6 Trapdoor experiment setup scheme. (Iglesia et al, 2011)

A system of wedges activates the movement in the trapdoor, as drawn in the scheme of Figure 3.6. The lower wedge moves horizontally and is attached to a displacement transducer. Due to lateral constraints, the upper wedge follows the lower wedge movement

sliding in vertical direction at a velocity of 0.18 mm/s. Trapdoor displacement is calculated by geometric relations.

Three 6.35 mm-thick aluminum pieces form the trapdoor strip, the middle one is 102 mm long and the others 76.2 mm. Each one is placed above a roller in one edge and a ball in one third of its length from the other edge. Load-cells are installed below the balls, however, only second segment data is considered. Figure 3.7 shows a scheme of the trapdoor.

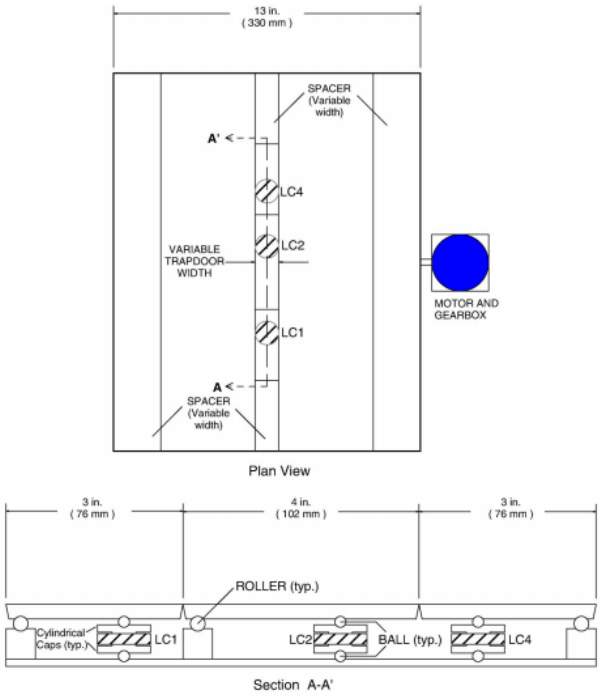

Figure 3.7 Trapdoor scheme. (Iglesia et al, 2011)

The geotechnical centrifuge used for these experiments is a Genisco apparatus with an effective radius of about 1.7 m, a payload capacity of 667 N and operable at up to 200*g* of centripetal acceleration.

1.3.2 Granular Material

Two types of granular material were employed for the tests, New Jersey 4/14 sand and glass beads.

<u>New Jersey 4/14 sand</u>

Numbers 4 and 14 indicate the U.S. standard sieves through particles pass and are retained. Its parameters are:

- Specific gravity (G_s) 2.66

- Average particle size 2.1 mm
- Uniformity coefficient C_u 1.7
- Minimum and maximum dry densities 1330 kg/m^3 and 1860 kg/m^3
- Minimum and maximum void ratios 0.43 and 1
- Peak friction angle of soil 39°

Peak friction angle was determined for a void ratio of 0.7 and normal stress level at 49 and 98 kPa.

Glass beads

Glass beads were used to investigate effects of scaling grain size with *g* level. Four major sizes were used: 0.5, 1.5, 3.0 and 6.0 mm. Chemical composition of beads included silica, soda and other materials. Its parameters are:

- Specific gravity (G_s) 2.55
- Young modulus of elasticity 14.3 GPa
- Poisson's ratio 0.27
- Rockwell hardness 47
- Average peak friction angle 28.5°

3.3.2. Tests Performed and Results

Soil is poured and scattered manually and the average bulk density is around 1600 kg/m^3 corresponding to a relative density of 60%. Ten tests were carried out with New Jersey sand, considering 1, 2 and 2.5 *H/B* ratios at 40*g* and 80*g*.

The test results are presented in normalized ratios for loading (P/P_0) and displacement (δ/B). A typical loading versus displacement plot is presented in Figure 3.8. At the start actuation of door movement, the normalized loading is 1.5 because of the higher stiffness of the trapdoor material. However, the load reaches the geostatic value (P/P_0 equals 1) with minimal displacement.

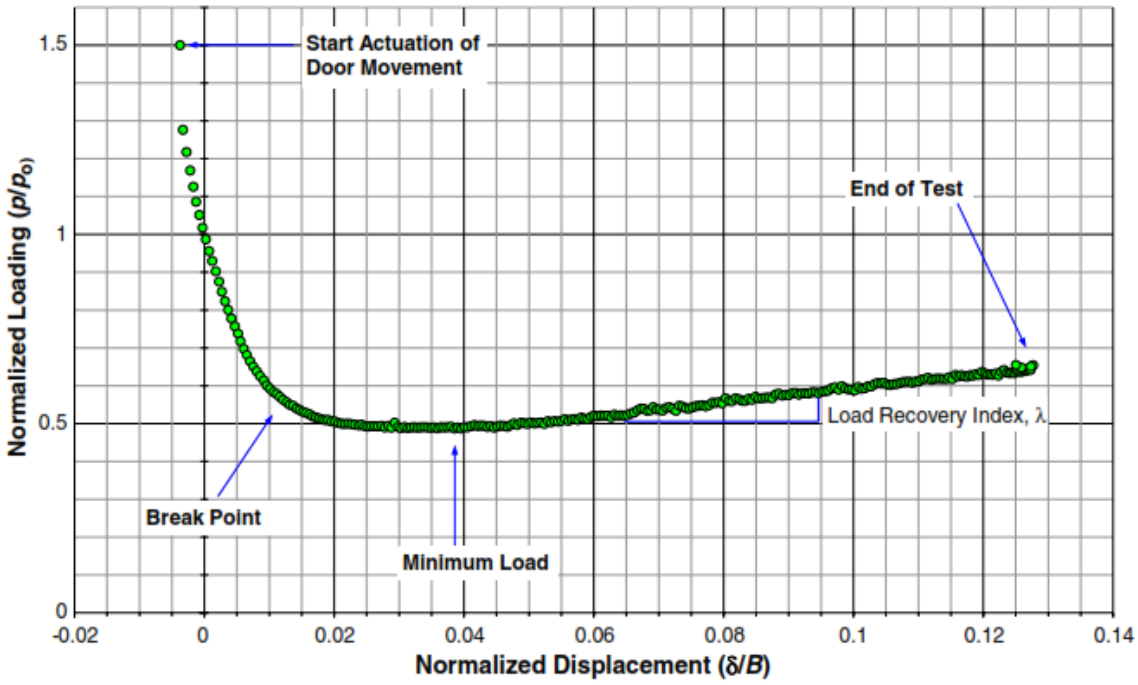

Figure 3.8 Typical loading versus displacement plot (Iglesia et al, 2014)

The point of maximum curvature is denominated break point and represents a change in loading behaviour. Normalized loading drops rapidly to this point and then the rate of load decrease greatly diminishes until minimum load point. Afterwards, load increases up to the end of the test, where the trapdoor cannot be moved down any further. Appendix 1 contains the table of results for every test performed by Iglesia et al (2011).

A plot with the four main state points (initial condition point, break point, minimum load point and end of the test point) for every test carried out, including glass beads, is presented in Figure 3.9. Two moduli of arching were estimated, tangent, taking in account the initial condition point, and secant, taking in account the break point, whose values are approximately 125 and 63 respectively. Also, the normalized displacement δ/B related to the minimum load point is found between 0.02 and 0.06.

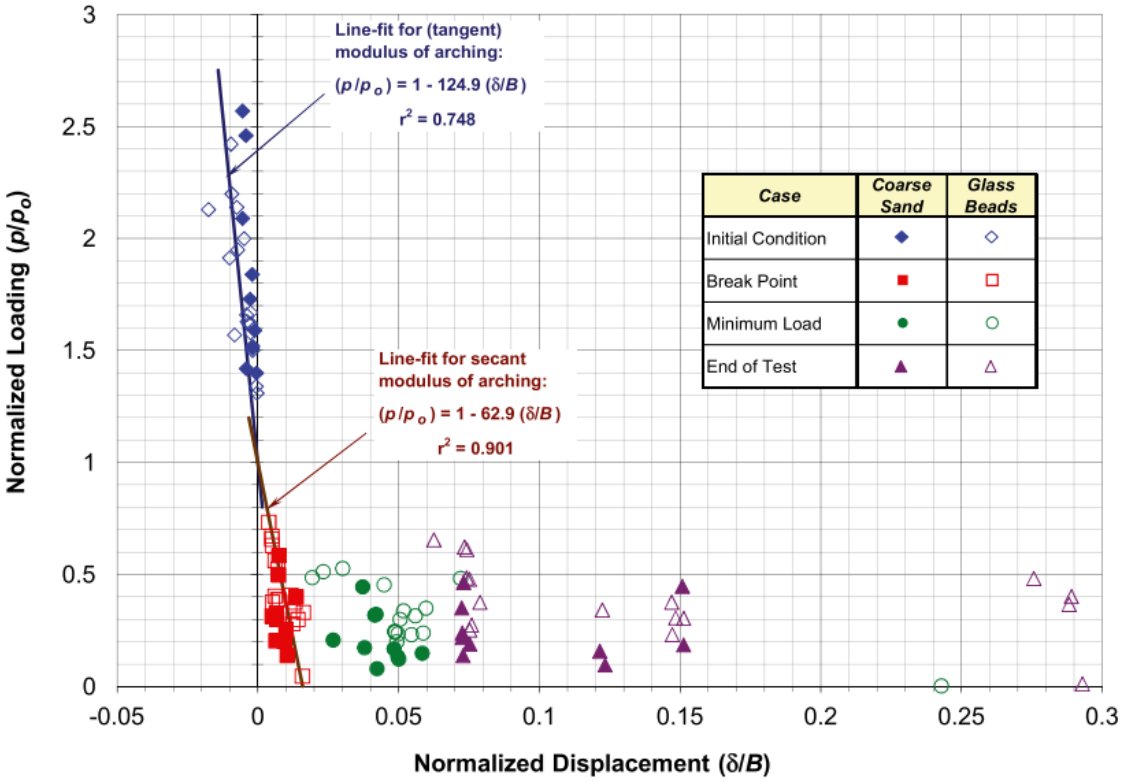

Figure 3.9 Results obtained with centrifuge test carried out by Iglesia et al (2014).

Results of geometrically similar experiments tested at properly scaled *g* levels succeeded in performing the same loading behaviour, as shown in Figure 3.10.

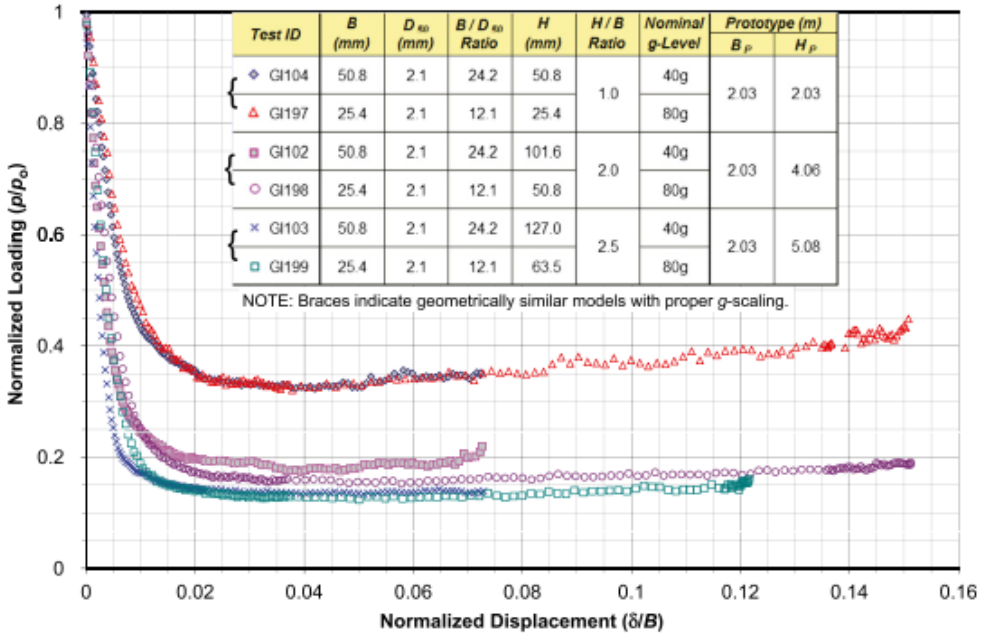

Figure 3.10. Tests with sand with different model sizes and g levels. (Iglesia et al, 2014)

Soil height variation over the trapdoor was analyzed with a 25.4 mm-wide trapdoor at approximately 80*g* level, as shown in Figure 3.11. The main remarks presented by Iglesia et al (2014) are summarized:

- Minimum absolute stress is the same for the four models, which accounts for the formation of a physical arch.
- Minimum load decreases as *H/B* ratio increase, which is compatible with the same value of minimum absolute stress for the four models.
- Break point load is greater than end of the test loading ratio except for *H/B*=1. According to previous research, a lower limit for substantial stress redistribution above the trapdoor falls between 1.5 to 2 *H/B* ratio.
- Normalized trapdoor displacement δ/B related to minimum load falls between 0.04 and 0.05 while break point loading is at 0.01 approximately.

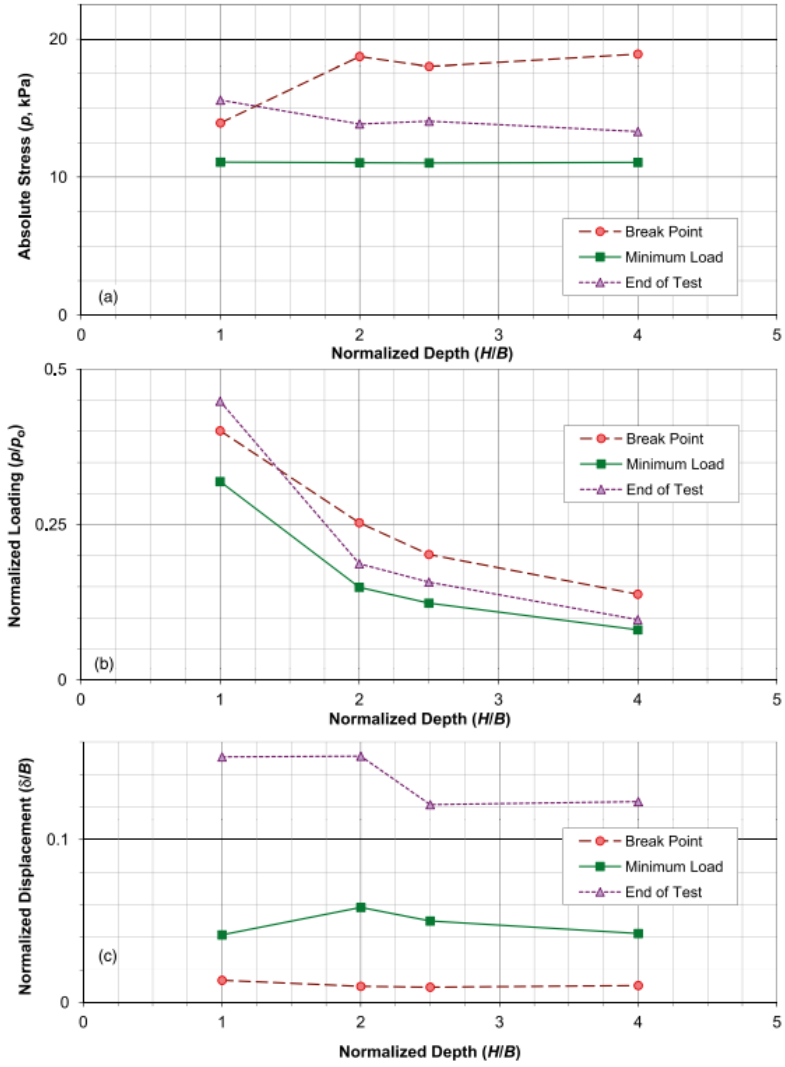

Figure 3.11 Effect of soil height variation. (Iglesia et al, 2014)

Table 3.1 shows the values used in Figure 3.11, corresponding to experiments GI197, GI198 and GI199, reported in Iglesia et al (2011) and Table 3.2 the theorical values for soil arching. In these experiments where a trapdoor of 25.4 mm long was employed and for every normalized ratio, the minimum load was below theorical value for parabolic arch.

Table 3.1 Normalized loading of pivotal states for GI197, GI198 and GI199 experiments carried out by Iglesia et al (2011).

	Break Point		**Minimum Load**		**End of the Test**	
H/B	P_m/P_0	δ/B **(%)**	P_m/P_0	δ/B **(%)**	P_m/P_0	δ/B **(%)**
1	0.400	1.4%	0.320	4.1%	0.450	15.1%
2	0.250	1.0%	0.150	5.0%	0.190	15.1%
2.5	0.200	0.9%	0.120	5.0%	0.160	12.6%

Table 3.2 Theorical minimum load values for soil arching considering a friction angle of 39°.

H/B	P_m/P_0 **parabola**	P_m/P_0 **triangular**	P_m/P_0 **intermediate**
1.0	0.360	0.395	0.714
2.0	0.186	0.199	0.357
2.5	0.150	0.160	0.286

Regarding soil deformation patterns, surface formations were practically unnoticeable whereas a limited volume of material follows the trapdoor displacement. And finally, according to test observations, for small relative displacements a curved arch will occur, followed by a triangular shaped arch for medium relative displacements, and finally, large relative displacements mobilize a prism of soil.

4. The Trapdoor Experiment Modelling

In the following sections, MPM code is used to simulate the yielding trapdoor test in granular soils on a geotechnical centrifuge. The experiment parameters employed in Iglesia et al (2014) have been taken as reference for the MPM base model and results will be compared with theirs.

4.1. Introduction

The yielding trapdoor test is used to study soil arching development in granular soils. Active soil arching occurs when the trapdoor begins to displace vertically downwards and stress redistribution is triggered. Load in the trapdoor decreases while the adjacent soil stresses increase. As movement continues, the trapdoor load drops rapidly and then stabilizes reaching a minimum value, which is associated to the soil arching mechanism. Such mechanism initiates as a parabolic slip surface over the trapdoor that turns into a triangular-shaped surface as relative displacement increases. As a result, trapdoor loading rate starts to rise. Ultimately, for large displacements, vertical slip surfaces develop at the edges and prism of soil is mobilized.

In an effort to quantify and study soil arching, Iglesia et al (2014) reported an analysis of the results of a series of trapdoor experiments using New Jersey 4/14 sand and glass beads, performed on a geotechnical centrifuge. Their main findings include the following:

- Four pivotal states in loading behaviour: initial conditions point, break point, minimum load point and end of the test point.
- Secant and tangent moduli of arching.
- Average normalized trapdoor displacement related to break point and minimum load point.
- Same minimum absolute stress for varying soil depths given a fixed width of trapdoor.

An MPM model has been developed in order to simulate one trapdoor test performed by Iglesia et al (2014) in dry sand at 40*g* level. Parameters used in the experiment have been taken as reference. Loading behaviour predicted by MPM is compared with the Iglesia et al (2014) main investigation findings.

4.2. Base Model Description

4.2.1. Geometry

A scheme of the model is showed in Figure 4.1, which consists of three basic elements: a soil layer, a trapdoor and a void zone below the soil. The values for each parameter are presented in Table 4.1.

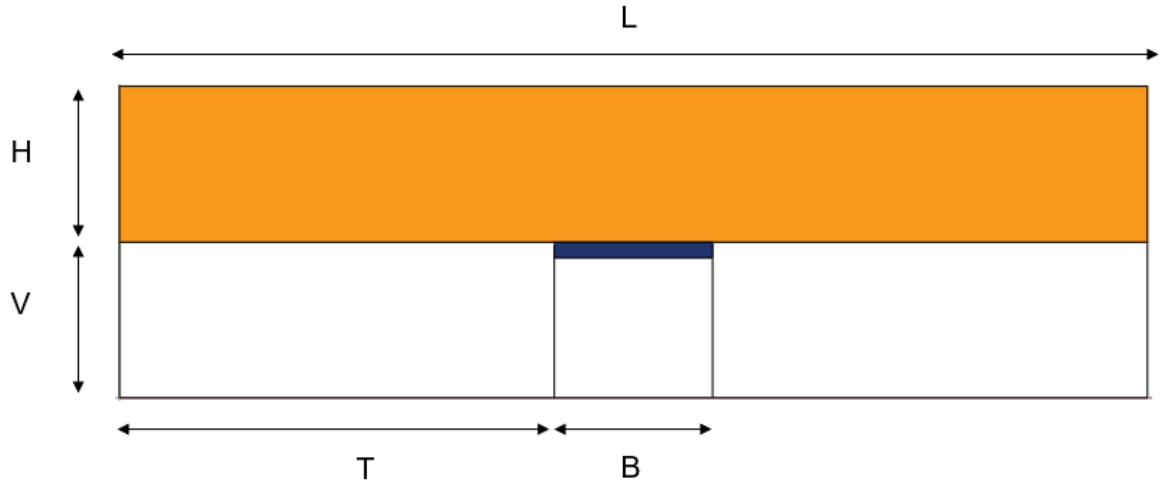

Figure 4.1 Scheme of base model.

Table 4.1 Base model geometry parameters.

Description	Symbol	Unit	Value
Soil layer height	*H*	m	0.05
Soil layer lenght	*L*	m	0.33
Soil layer thickness	*w*	m	0.01
Trapdoor lenght	*B*	m	0.0508
Void zone height	*V*	m	0.05
Distance to trapdoor edge	*T*	m	0.1396
Normalized depth ratio	*H/B*		1

4.2.2. Boundary Conditions

The model presents x-fixities at both lateral sides and total fixity at the bottom. Soil layer bottom has y-fixity. The trapdoor presents a prescribed vertical velocity of zero m/s instead of fixities for the quasistatic part of the simulation.

At the start of the dynamic stage, y-fixity between soil bottom and the top of the trapdoor is removed and trapdoor vertical velocity is set to -0.2 mm/s.

4.2.3. Materials

Soil behaviour was modelled with strain softening Mohr-Coulomb constitutive law presented by Yerro et al (2014). Linear elasticity model was employed to model trapdoor behaviour.

Table 4.2 Base model material parameters.

Material Paramaters	Unit	Soil	Trapdoor
Material Type		1 ph. Solid	1 ph. Solid
Porosity Solid		0.35	0

Material Paramaters	Unit	Soil	Trapdoor
Density Solid	kg/m^3	2700	2000
K0 Value Solid		0	0
Intrinsic Permeability Solid	m^2	0	0
Material Model Solid		SS MC	Linear Elasticity
Young Modulus	kPa	5000	50000
Poisson Ratio		0.35	0.33
Peak Cohesion	kPa	0.1	
Residual Cohesion	kPa	0.1	
Peak Friction Angle	°	35	
Residual Friction Angle	°	30	
Peak Dilantancy Angle	°	0	
Residual Dilantancy Angle	°	0	
Shape Factor η		500	

A low Young modulus was used for soil in order to reduce computational time. Although the sand employed in trapdoor experiments performed was cohesionless, a very low (0.1 kPa) peak and residual cohesion was assigned to the soil to significantly reduce calculation time.

4.2.4. Loading Conditions

Gravity multiplier is applied from 0 to 40 at the quasistatic stage by 10 load steps of 1 s each and is maintained at this level throughout the dynamic stage.

4.2.5. Mesh

An unstructured mesh of 0.01-m long tetrahedral elements was used for the model. Also, 4 material points were assigned to each element. Mesh dependency is expected in MPM and will be further studied with the parametric study. Figure 4.2 shows the mesh and material point distribution used in the simulation.

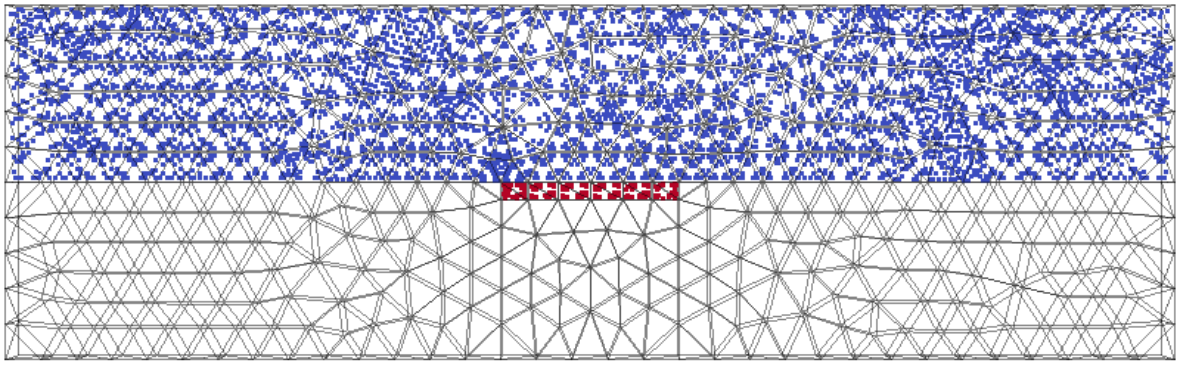

Figure 4.2. Mesh and material point distribution for base model.

4.2.6. Numerical parameters

For the quasistatic and dynamic stages, damping factors of 0.75 and 0.05 are used respectively.

4.3. Base Model Quasistatic Results

Figure 4.3 and 4.4 present the effective vertical and horizontal initial stress for the soil layer.

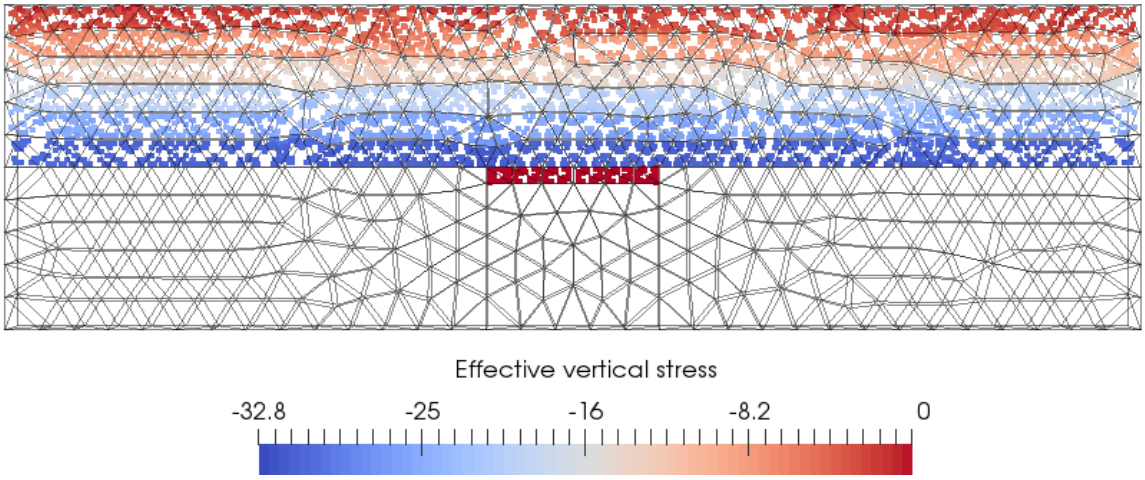

Figure 4.3 Initial Effective Vertical stress (kPa).

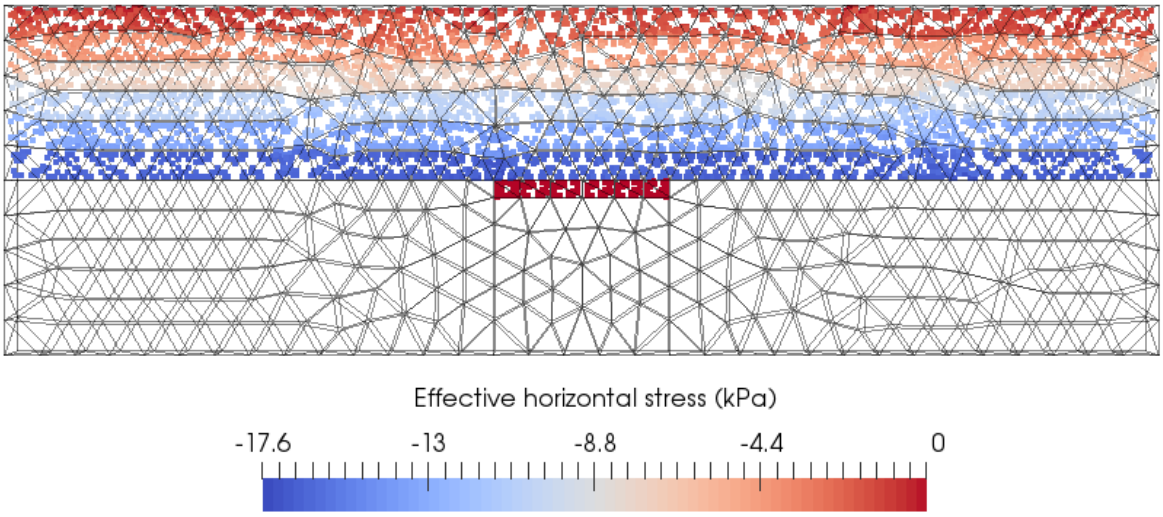

Figure 4.4 Initial Effective Horizontal stress (kPa).

4.4. Base Model Dynamic Results

For the dynamic stage, 30 steps of 1 second were simulated. Trapdoor displacement δ reached 0.006 m, which corresponds to a normalized displacement δ/B of 11.8%.

4.4.1. Effective Vertical Stress Evolution

Twelve material points were selected in order to the study vertical stress evolution over the yielding trapdoor. Figure 4.5 shows selected points and Table 4.3 presents their geometric coordinates. The *n* variable equals the relative horizontal distance from each material point to the left edge of the trapdoor, according to the following expression $n = (X_{MP} - T)/B$.

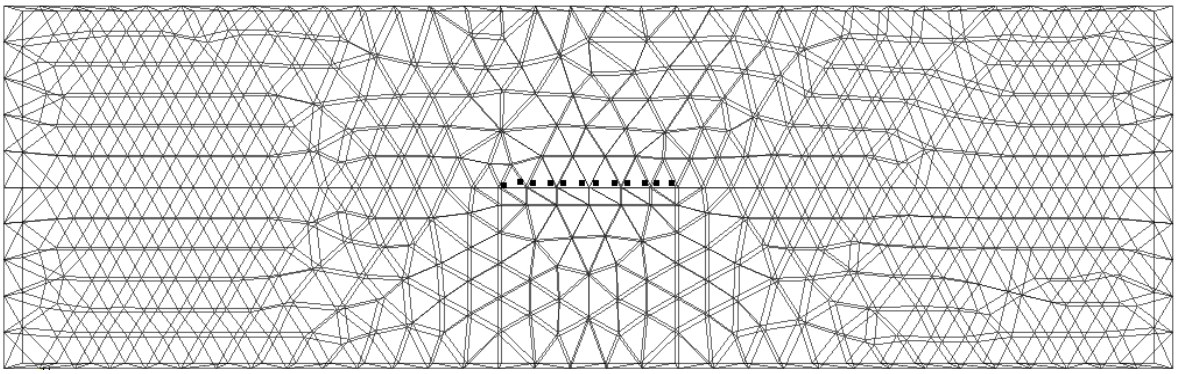

Figure 4.5 Material points selected for effective vertical stress evolution analysis over the trapdoor for base model.

Table 4.3 Material point geometric parameters used for effective vertical stress analysis over the trapdoor.

MP	X (m)	Y (m)	Z (m)	*n*
227	0.1407	0.0506	0.0022	0.02
288	0.1456	0.0515	0.0067	0.12
772	0.1490	0.0511	0.0058	0.19
760	0.1540	0.0510	0.0040	0.28
1056	0.1578	0.0511	0.0040	0.36
992	0.1633	0.0512	0.0059	0.47
956	0.1671	0.0512	0.0059	0.54
972	0.1725	0.0512	0.0041	0.65
628	0.1762	0.0551	0.0059	0.72
2993	0.1811	0.0512	0.0072	0.82
241	0.1844	0.0511	0.0086	0.88
240	0.1888	0.0511	0.0059	0.97

The average trapdoor displacement δ versus time is presented in Figure 4.6. Material point 227 reached the bottom of the model at time step 39 and was not taken in account for the average trapdoor displacement nor the average stresses of the two last time steps.

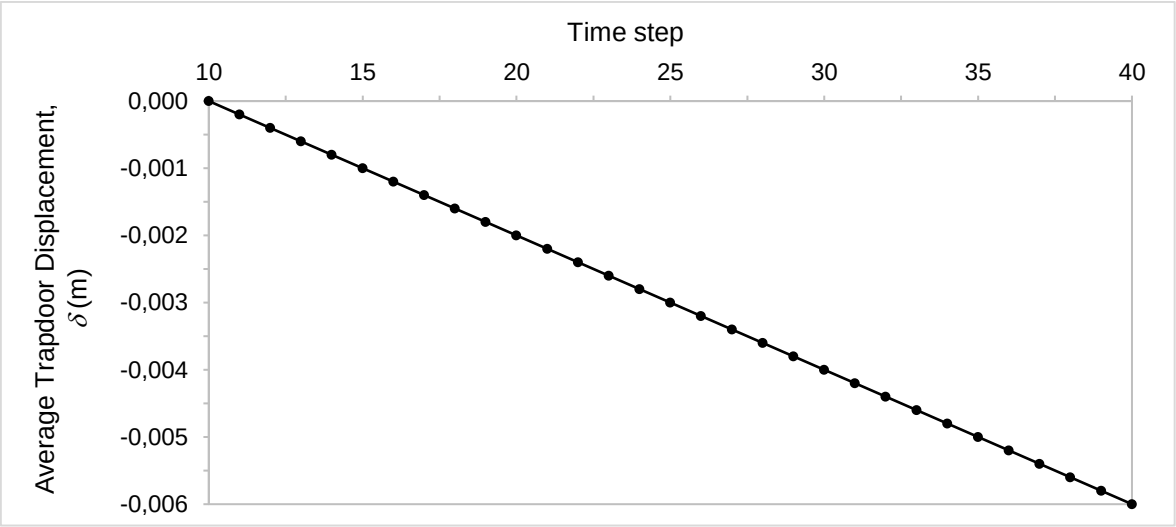

Figure 4.6 Average Trapdoor Displacement vs Time Step.

In order to calculate the average load P_m on the trapdoor for every time step, the effective vertical stress was obtained for every material point at each time step and then the simple mean of the twelve values was calculated. Figure 4.7 presents the evolution of the vertical stress distribution throughout the 40 time steps, where it can be appreciated that the ratio of load decrease is not uniform. Faster ratios are triggered at the vicinity of the trapdoor edges, whereas at the middle zone presents the lowest ratios.

Figure 4.7 Effective Vertical Stress σ'_y for each time step versus Relative Distance to Trapdoor Left Edge n for base model. Initial time steps are dark gray colored.

The normalized loading P_m/P_0 is then calculated, where P_0 is the average geostatic stress on the trapdoor. Figure 4.8 shows the normalized loading versus normalized displacement plot. The normalized loading for the break point is estimated in 0.584 at a relative displacement of 1.2% which yields a secant arching modulus of 35.2, while the minimum normalized loading is 0.503 at a normalized displacement of 9.1%. Break point normalized displacement is compatible with Iglesia et al (2014) results where 1% was found to be the average value. End of the test point presents P_m/P_0 of 0.551 at a δ/B of 11.8%. Loading behaviour is the expected up to 7% of normalized displacement, when the ratio starts to decrease. If the rise was sustained, the minimum load point would correspond to a P_m/P_0 of 0.504 at δ/B of 2%, quite close to 0.503.

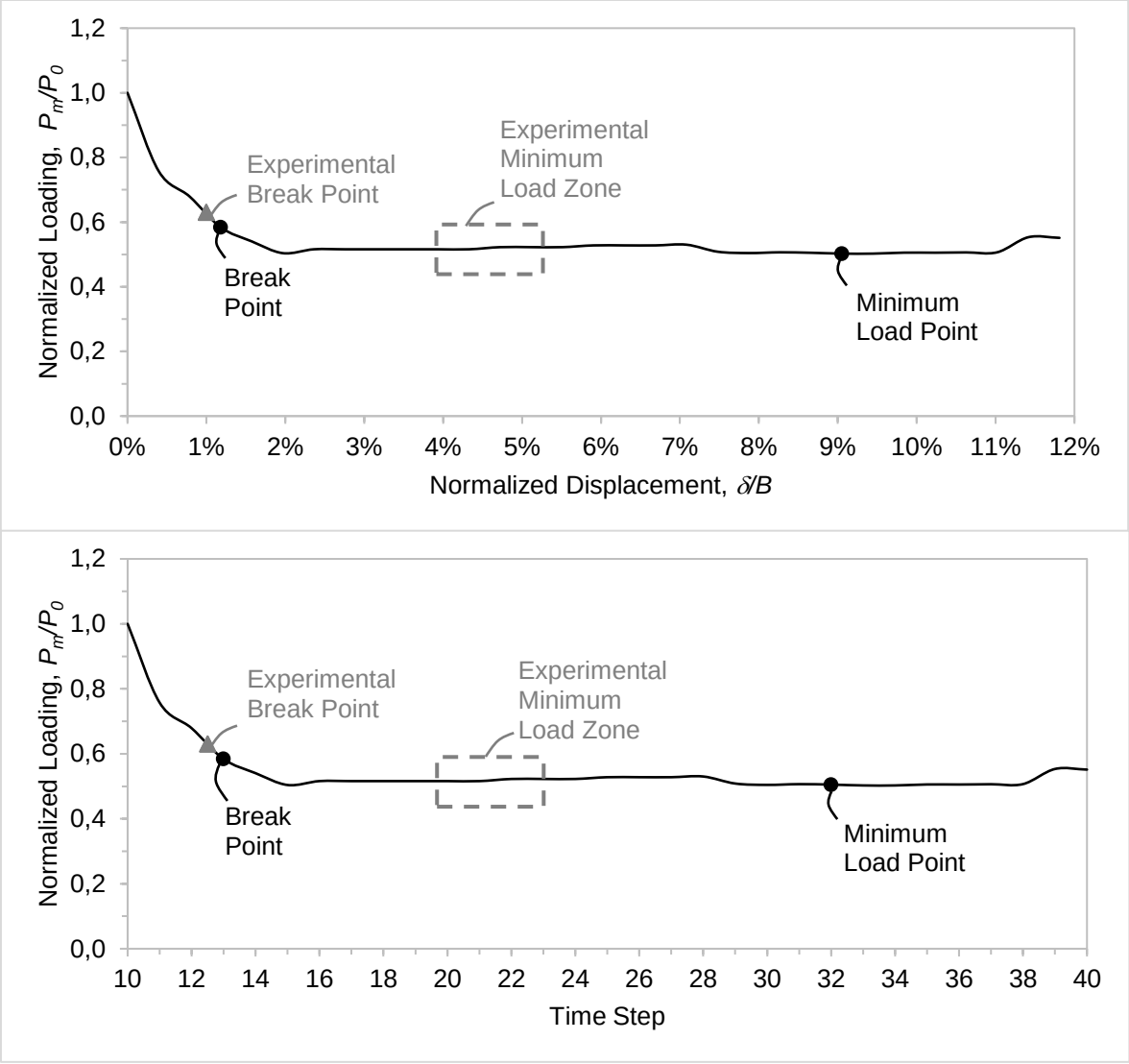

Figure 4.8 (a) Normalized Loading P_m/P_0 versus Normalized Displacement δ/B for base model. (b) Normalized Loading P_m/P_0 versus time step for base model.

Table 4.4 and 4.5 present theorical values for minimum normalized loading and soil weight below the arch respectively, using Iglesia et al (2014) formulas, and Table 4.6 shows results

obtained with MPM base model. The MPM minimum load and soil weight fall between theorical values of triangular arch for peak and residual friction angle.

Table 4.4 Minimum normalized loading P_m/P_0 estimation according to Iglesia et al (2014) proposed formulas for soil arching, considering peak and residual values for friction angle of 35° and 30°.

	K_E	P_m/P_0 parabola	P_m/P_0 triangular	P_m/P_0 intermediate
Peak	0.505	0.394	0.445	0.691
Residual	0.600	0.443	0.521	0.662

Table 4.5 Theorical values for soil weight below the parabolic and triangular arch, considering peak and residual values for friction angle of 35° and 30°.

	$W_{parabola}$ (kN)	$W_{triangular}$ (kN)
Peak	6.77	10.15
Residual	8.21	12.31

Table 4.6 Results for minimum normalized loading P_m/P_0 and weight below soil arch obtained with MPM for base model.

P_m/P_0 MPM	W_{MPM} (kN)
0.503	12.7

4.4.2. Soil Layer Deformation and Slip Surfaces

According to Iglesia et al (2014), a triangular shaped arch is formed above the trapdoor considering medium normalized displacements. This mechanism was checked with deviatoric strain, and horizontal displacement plots (Figure 4.9 and 4.10). The triangle height was measured directly from deviatoric strain plots and was 0.034m high, which is close to the rise of the arch ($B\cot\varphi/2$) for peak friction angle, 0.036m. The parabolic arch was not clearly identified in this plot; however, its height could be approximately measured in the horizontal displacement plots, giving 0.014m while theorical arch rise ($B\tan\varphi/4$) for peak friction angle is 0.018m. Table 4.7 summarizes these values.

Table 4.7 Soil arch height for parabolic and triangular shapes according to Iglesia et al (2014) considering peak and residual values for friction angle of 35° and 30° and base model arch height results.

	Soil arch height (m)	
	Parabolic	**Triangular**
Peak	0.018	0.036
Residual	0.022	0.044
MPM	0.014	0.034

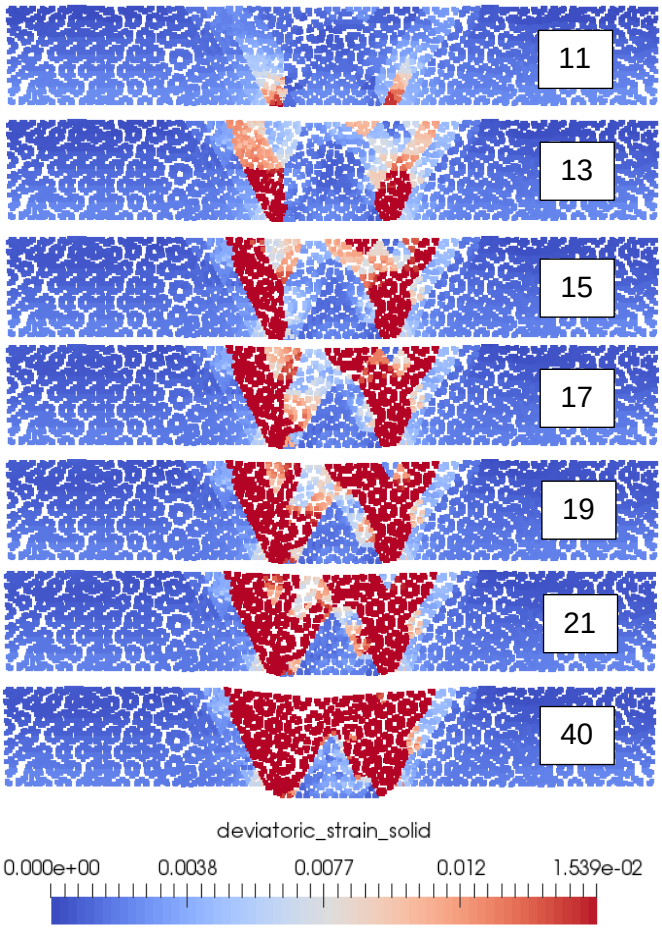

Figure 4.9 Deviatoric Strain Evolution for base model. Time step is shown in each plot.

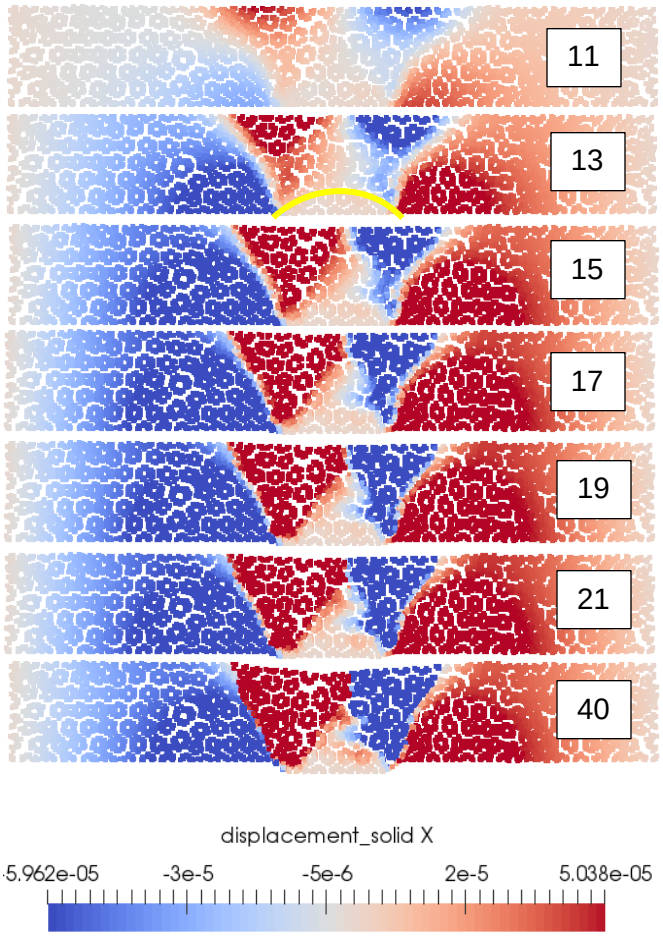

Figure 4.10 Horizontal Displacement evolution for base model. Time step is shown in each plot.

Two external slip surfaces stem from both edges of the trapdoor with an angle of 66.3°, close to Rankine's angle for an active rupture surface ($45° + \frac{\varphi}{2}$) which value is 60° for a friction residual angle of 30°. In addition, the external angle with the vertical of the triangle arch was measured in 30.7°, close to friction residual angle.

Surface settlements were triggered as can be seen in time step 40 in both plots. The largest value was 5.26 mm.

4.4.3. Effective Horizontal Stresses

A set of material points at the bottom of the soil layer were selected in order to study the evolution of effective horizontal stress (Figure 4.11) and the distance of each point to the left side of the model was normalized with a similar criterion used for vertical stresses, in this case $m = X_{MP}/T$ (Table 4.8).

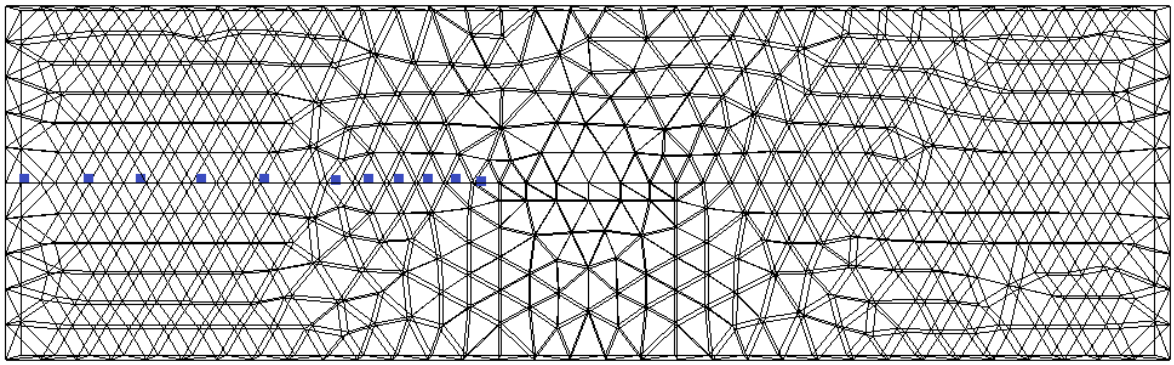

Figure 4.11 Material points selected for effective horizontal stress evolution analysis for base model.

Table 4.8 Material point geometric parameters used for effective horizontal stress.

MP	X (m)	*m*
310	0.1341	0.96
514	0.1186	0.85
722	0.1101	0.79
818	0.1013	0.73
2401	0.0923	0.66
1582	0.0731	0.52
4785	0.0532	0.38
1480	0.0377	0.27
1881	0.0220	0.16
4626	0.0014	0.01

Figure 4.12 shows that stresses increase up to time step 15, which corresponds with the break point, and then the rate of increase abruptly diminishes. Also, as points approach the trapdoor edge, the effective horizontal stress is greater. Moreover, in Figure 4.13, material point 514 presents the highest peak of said stress, reaching up to 44 kPa or 2.6 times the quasistatic stress.

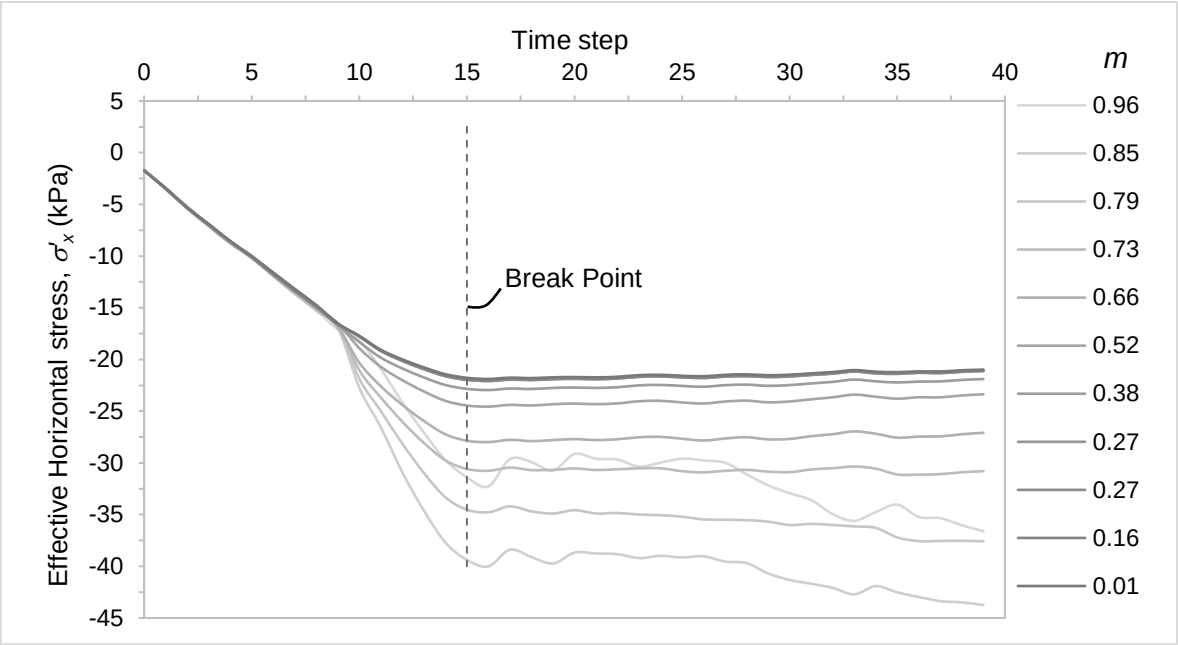

Figure 4.12 Effective Horizontal Stress σ'_x versus Time Step for base model.

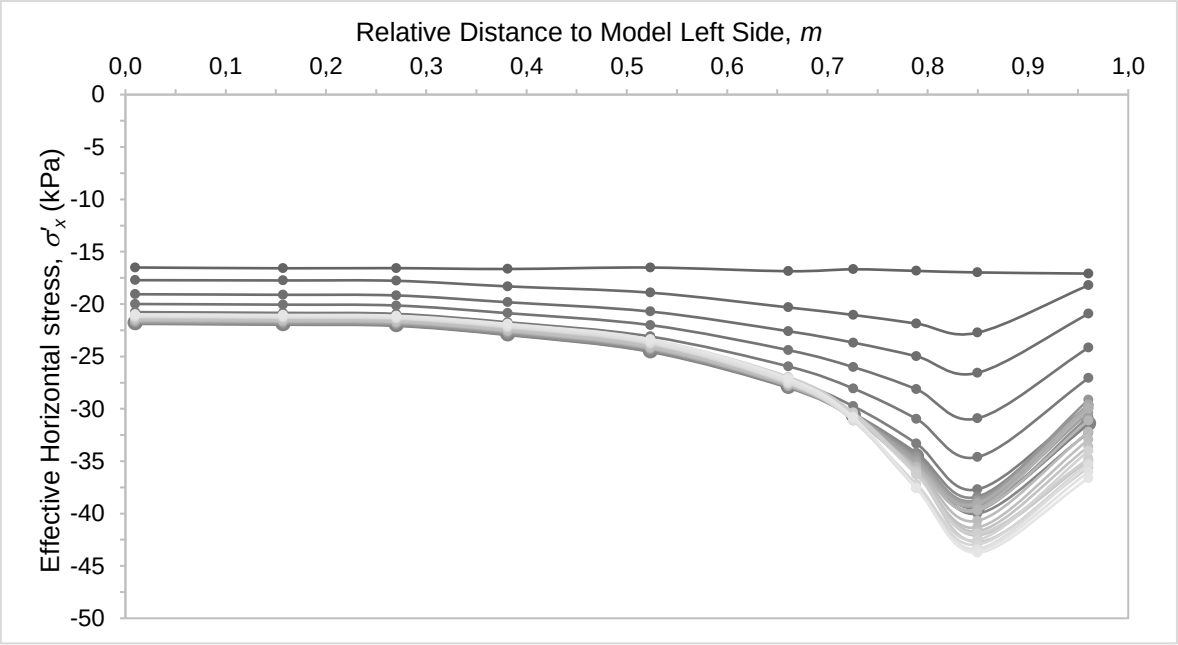

Figure 4.13 Effective Horizontal Stress σ'_x versus Relative distance to Model Left Side, *m*, for base model. Dark grey color is used in firsts time steps.

5. Parametric Study

In this chapter, a parametric study of soil parameters regarding the main variables of the yielding trapdoor is carried out. Results are compared with a base model developed with MPM code.

5.1. Introduction

Yielding trapdoor experiments are carried out to study soil arching effect. Iglesia et al (2014) reported and analyzed the results of a series of trapdoor experiments on a geotechnical centrifuge in order to study this phenomenon. A base model was developed in MPM code taking in reference the parameters of one of said experiments with a normalized depth *H/B* of 1 on 40*g* level. According to Iglesia et al (2014), the minimum absolute stress on the trapdoor is independent of normalized depth, therefore this effect was studied with three different soil layer heights. In addition, mesh element size as well as peak and residual friction angle variation effect were studied. Table 5.1 presents a list of the models and its main parameters.

Table 5.1 List of models for parametric study of yielding trapdoor experiment

Name	*H/B*	ϕ_p	ϕ_r	Mesh element size (m)
Base model	1	35	30	0.01
H2	2	35	30	0.01
H2.5	2.5	35	30	0.01
M5	1	35	30	0.005
M8	1	35	30	0.008
F1	1	40	35	0.01
F2	1	45	40	0.01

5.2. Normalized Depth *H/B*

As Figure 5.1 shows, loading behaviour is similar in the three cases, for normalized displacements up to 2% a quick drop of the normalized loading is seen and for further trapdoor movement, the rate of decrease greatly diminishes. Also, as *H/B* increases, P_m/P_0 stabilizes at lower values. For *H/B* of 2 and 2.5 a slight tendency of load increase is reported from approximately 7% of δ/B to the end of the test.

In order to study the evolution of effective vertical stresses on the trapdoor, material points with the same location were selected in H2 and H2.5 models. Figure 5.2 presents σ'_y for each material point at minimum load time step. The stress curve shape is similar in the three cases, however, the values increase for higher *H/B*.

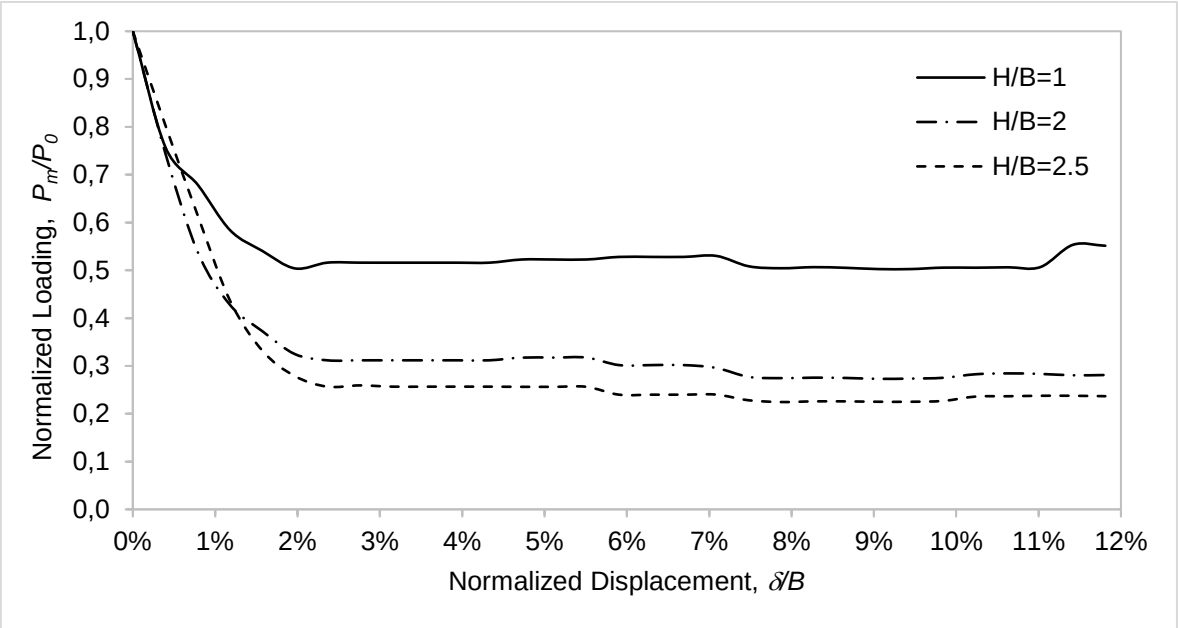

Figure 5.1 Normalized Loading P_m/P_0 versus Normalized Displacement δ/B for normalized depths H/B of 1, 2 and 2.5.

Figure 5.2 Effective Vertical Stress σ'_y for minimum load time step versus Relative Distance to Trapdoor Left Edge n for normalized depths H/B of 1, 2 and 2.5

Pivotal states were also analyzed, following Iglesia et al (2014) criterion. Figure 5.3 (a) shows the absolute stress for break point, minimum load and end of the test. In the three cases, end of the test stress falls between minimum load and break point. Minimum load increases with H/B, being 15.6, 17.8 and 18.3 kPa its values for normalized depth ratios of 1, 2 and 2.5 respectively. This does not match Iglesia et al (2014) main conclusion, and it

suggests that soil arch mechanism is not properly modelled with the given characteristics of the model.

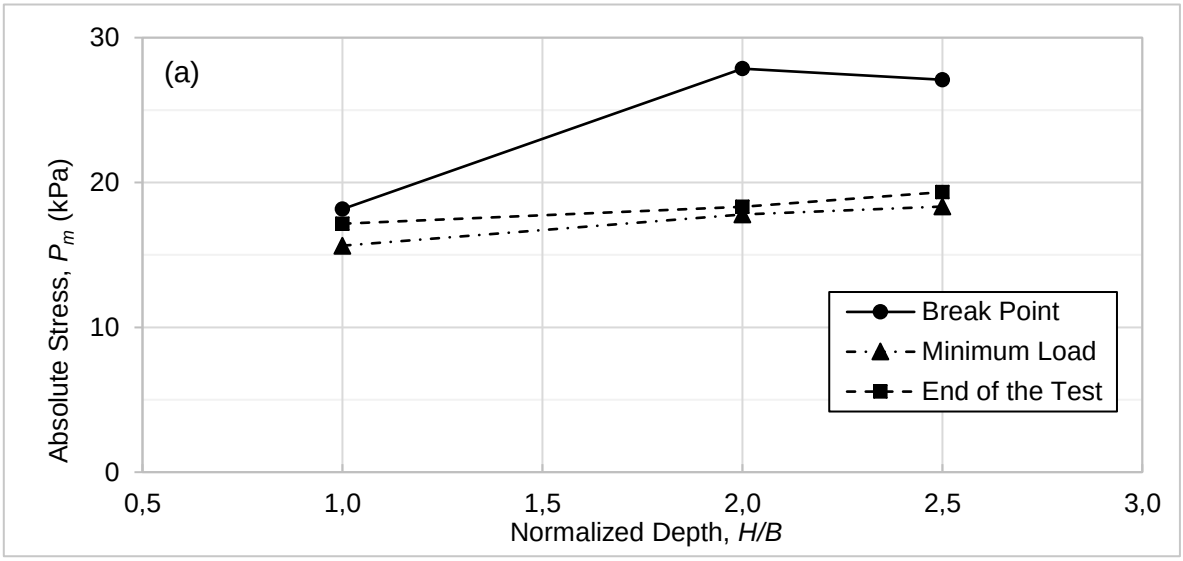

Figure 5.3 Absolute stress P_m versus Normalized Depth H/B.

Figure 5.4 shows the normalized loadings for pivotal states for each case. Great decrease of vertical load is presented for higher heights of soil, P_m/P_0 is 0.503, 0.273 and 0.225 for H/B of 1, 2 and 2.5 respectively.

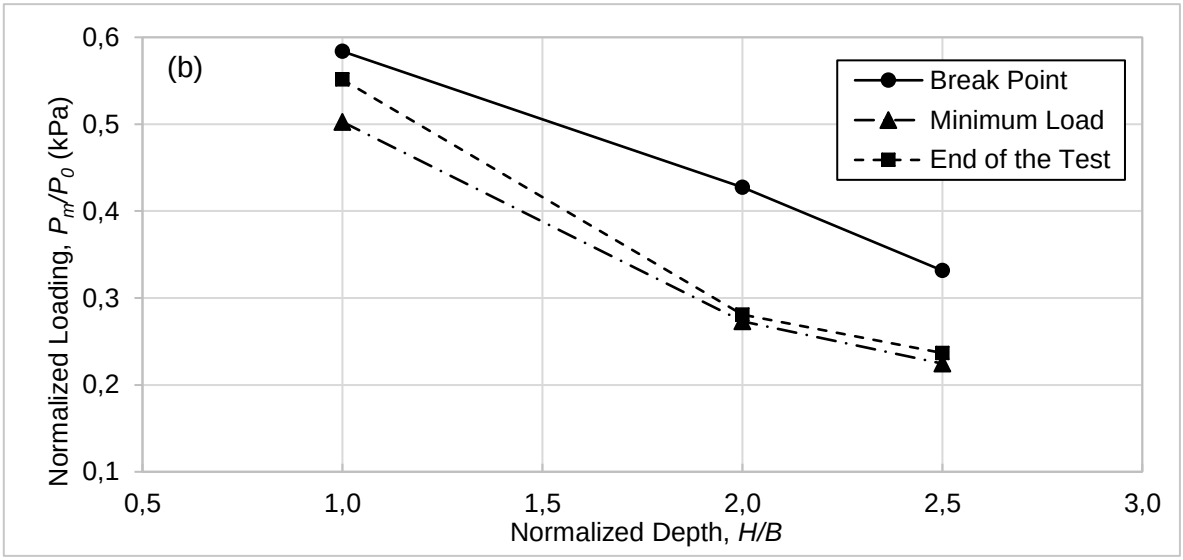

Figure 5.4 Normalized Loading P_m/P_0 versus Normalized Depth H/B.

Figure 5.5 presents normalized displacement versus normalized depth. Break point values of δ/B were 1.2%, 1.2% and 1.6% for H/B of 1, 2 and 2.5 respectively, which is close to the average displacement (1%) for this point reported by Iglesia et al (2014). However, δ/B for minimum load present larger values than the average (between 4% and 5%).

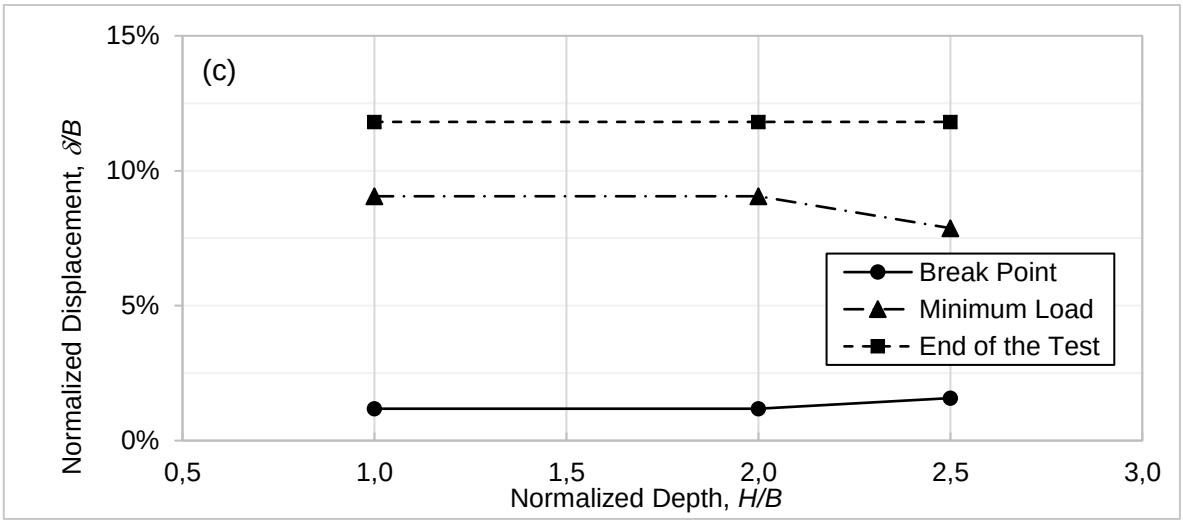

Figure 5.5 Normalized Displacement δ/B versus Normalized Depth H/B.

The values for minimum normalized loading ratio were calculated for every arch type, as shown in Tables 5.2 and 5.3 for *H/B* of 2 and 2.5. In both cases, each load falls between theorical values of triangular and intermediate terminal state for residual friction angle. Table 5.4 presents values for minimum load and weight below soil arch for every normalized depth. Weight increases for *H/B* of 2 and 2.5, which is directly related to absolute minimum stress.

Table 5.2 Minimum normalized loading P_m/P_0 estimation according to Iglesia et al (2014) proposed formulas for soil arching, considering peak and residual values for friction angle of 35° and 30° for *H/B*=2.

***H/B*=2**	K_E	P_m/P_0 parabola	P_m/P_0 triangular	P_m/P_0 intermediate
Peak	0.505	0.203	0.224	0.345
Residual	0.600	0.228	0.262	0.331

Table 5.3 Minimum normalized loading P_m/P_0 estimation according to Iglesia et al (2014) proposed formulas for soil arching, considering peak and residual values for friction angle of 35° and 30° for *H/B*=2.5

***H/B*=2.5**	K_E	P_m/P_0 parabola	P_m/P_0 triangular	P_m/P_0 intermediate
Peak	0.505	0.164	0.180	0.276
Residual	0.600	0.183	0.210	0.265

Table 5.4 Results for minimum normalized loading P_m/P_0 and weight below soil arch obtained with MPM for *H/B*=1, 2 and 2.5

H/B	P_m/P_0 MPM	W_{MPM} (kN)
1	0.503	12.7
2	0.273	14.5
2.5	0.225	14.9

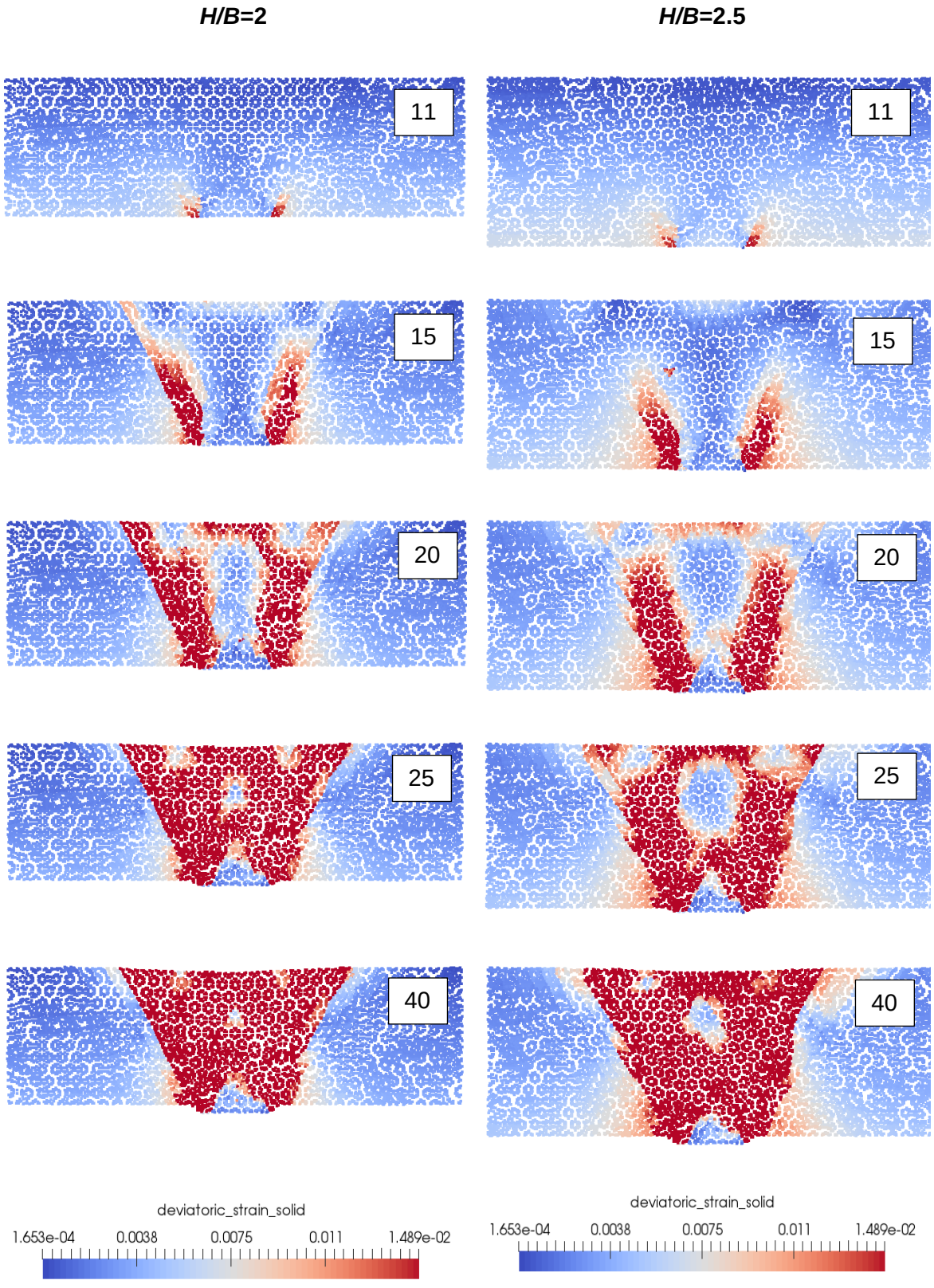

Figure 5.6 Deviatoric Strain Evolution for *H/B* 2 and 2.5. Time step is shown in each plot.

Figure 5.6 presents deviatoric strain evolution for *H/B* of 2 and 2.5. Plots show that two slip surfaces stem from each edge of the trapdoor and reach the surface at time step 20 approximately. The shape of the deformed soil is that of intermediate terminal state, which is compatible with the minimum load for both normalized depths. A triangle arch also develops over the trapdoor.

Figure 5.7 shows horizontal displacement plots for *H/B*=2 and 2.5. A parabolic arch is clearly present above the trapdoor. The height was directly measured from the plots. Table 3.7 shows arch heights for each normalized depth.

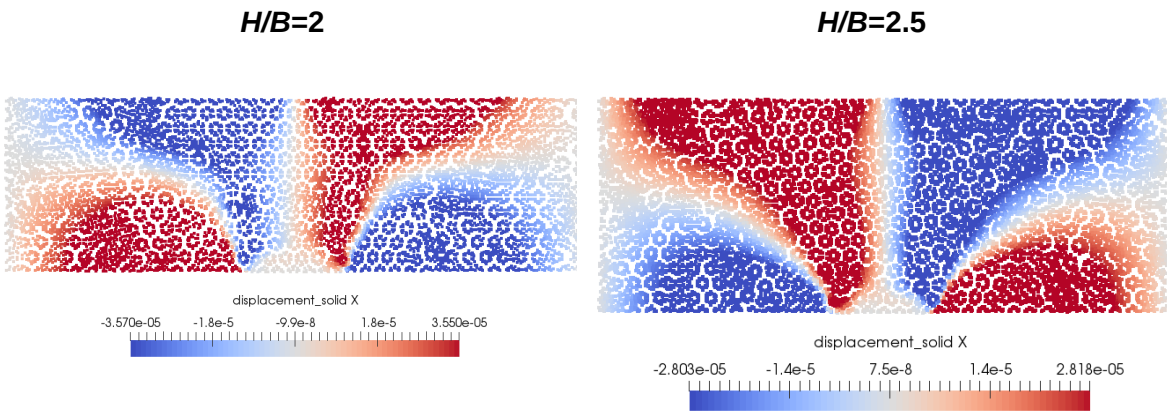

Figure 5.7 Horizontal Displacement for *H/B* 2 and 2.5 at time step 13.

Table 5.5 Soil arch height for parabolic and triangular shapes according to Iglesia et al (2014) considering peak and residual values for friction angle of 35° and 30 and heights *H/B*=1, 2 and 2.5.

	Soil arch height (m)	
	Parabolic	**Triangular**
Peak	0.018	0.036
Residual	0.022	0.044
***H/B*=1**	0.014	0.034
H/B=2	0.016	0.023
***H/B*=2.5**	0.014	0.030

5.3. Mesh Element Size

As Figure 5.8 shows, the loading behaviour is similar in the three cases, however, for the finer meshes load stabilizes at higher values. Table 5.6 presents pivotal states normalized loadings, break point load is 0.624 and 0.646 for 0.008 m and 0.005 m mesh size models respectively; furthermore, minimum load falls between triangular and intermediate terminal state (Table 4.4). Normalized displacement for break point is close to average reported by Iglesia et al (2014), but the values for minimum load do not fall between average range. Additionally, for 0.005 m mesh size, minimum load occurs at the end of the test. Figure 5.9 shows the effective vertical stress on the trapdoor for minimum load time step, where it can

be seen that for finer meshes, the stress in the left edge are substantially higher than for base model (-7.3 kPa and -18 kPa against 0 kPa).

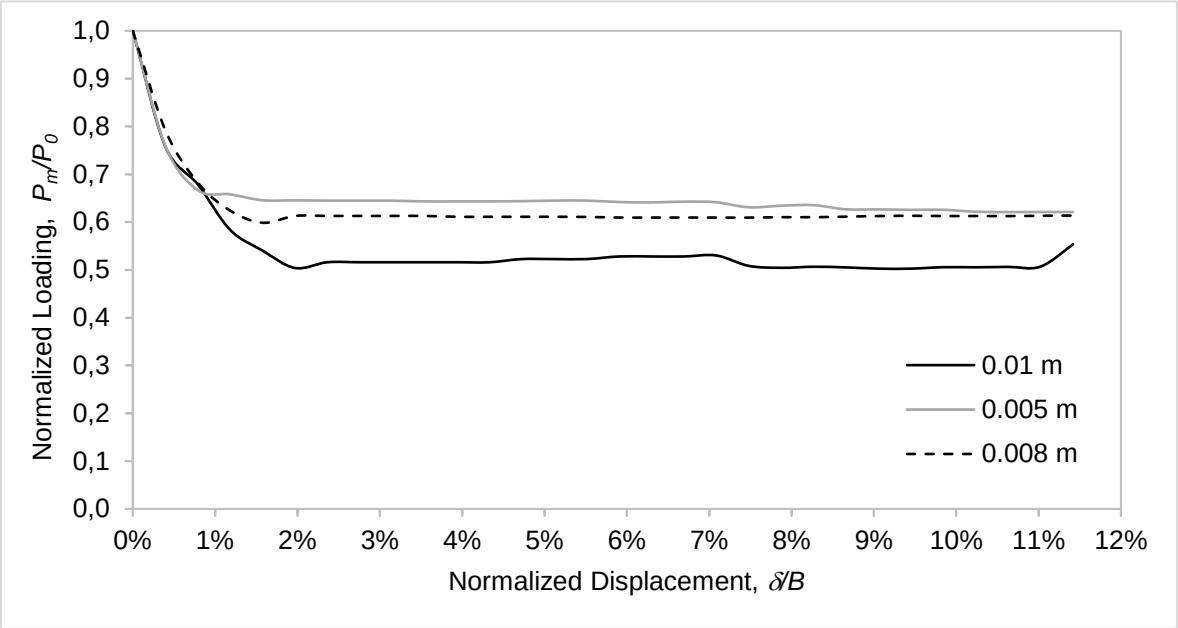

Figure 5.8 Normalized Loading P_m/P_0 versus Normalized Displacement δ/B for mesh sizes of 0.01 m, 0.008 m and 0.005 m.

Figure 5.9 Effective Vertical Stress σ'_y for minimum load time step versus Relative Distance to Trapdoor Left Edge n for mesh sizes of 0.01 m, 0.008 m and 0.005 m.

Table 5.6 Normalized loading of pivotal states for 0.01 m, 0.008 m and 0.005m mesh sizes.

	Break Point		Minimum Load		End of the Test	
Mesh (m)	P_m/P_0	δ/B (%)	P_m/P_0	δ/B (%)	P_m/P_0	δ/B (%)
0.01	0.584	1.2%	0.503	9.1%	0.551	11.4%
0.008	0.624	1.2%	0.599	1.6%	0.614	11.4%
0.005	0.646	1.6%	0.621	11.8%	0.621	11.8%

Figures 5.10 and 5.11 show deviatoric strain evolution for 0.008m and 0.005 m mesh size. In both cases, two slip surfaces are triggered and reach the surface at time step 12. The shape of the deformed soil is that of intermediate terminal state, which is compatible with the minimum load for both normalized depths. Afterwards, a triangle shape is formed above the trapdoor and surface settlements are present at final time step.

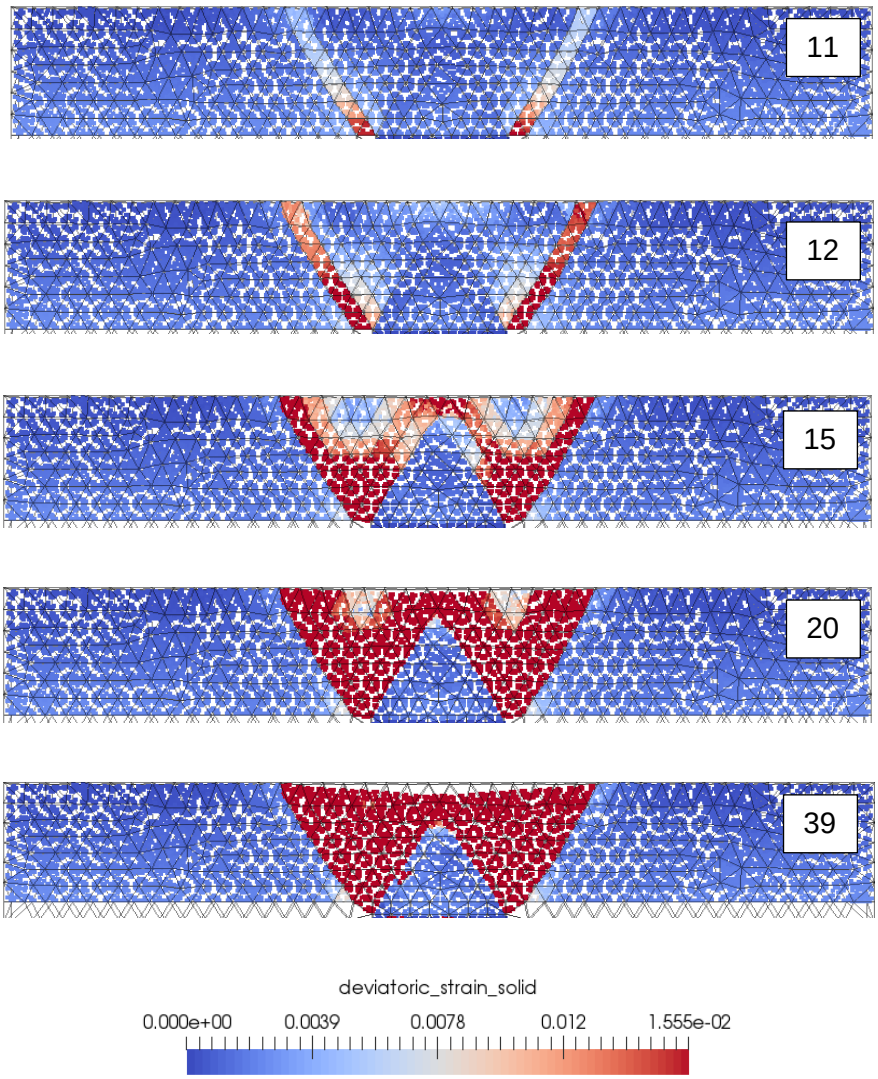

Figure 5.10 Deviatoric Strain Evolution for 0.008 m mesh size. Time step is shown in each plot.

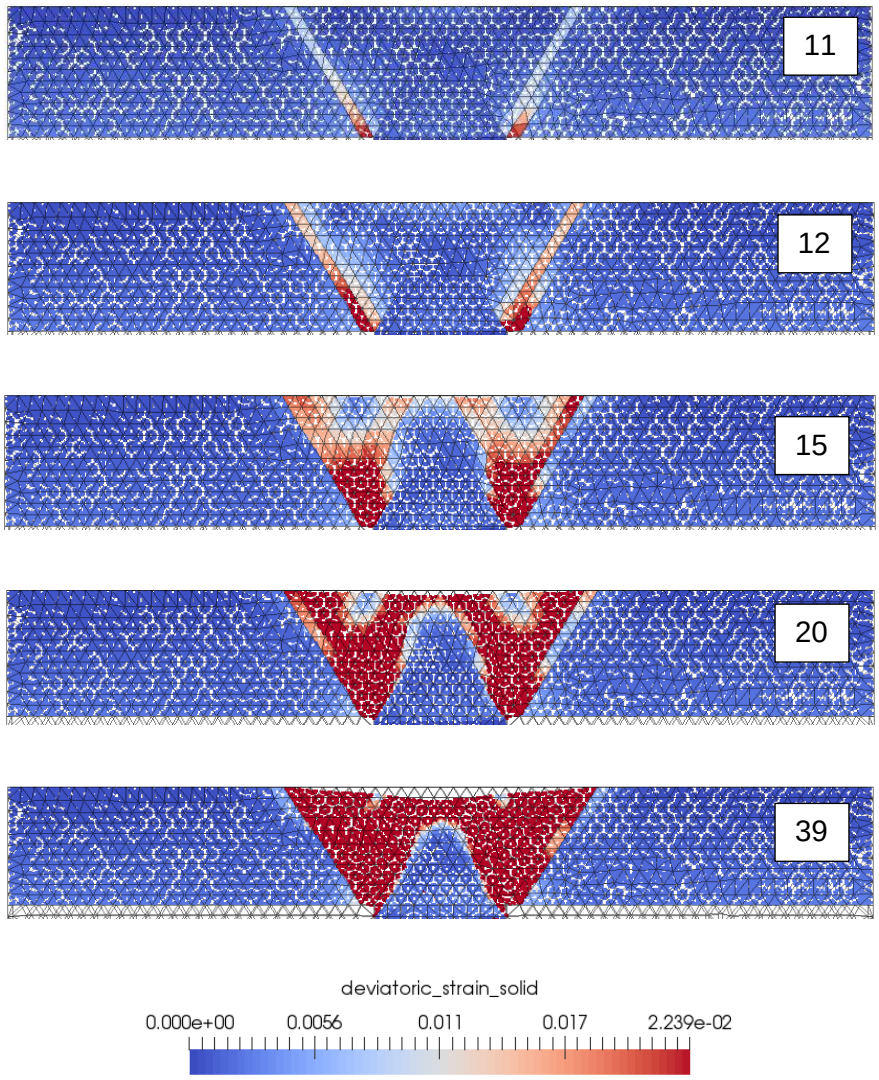

Figure 5.11 Deviatoric Strain Evolution for 0.005 m mesh size. Time step is shown in each plot.

As can be seen in Figures 5.12 and 5.13, horizontal displacement plots do not display a parabolic arch. Table 5.7 shows soil arch height for each model and values are close to theorical residual triangular height.

Table 5.7 Soil arch height for parabolic and triangular shapes according to Iglesia et al (2014) considering peak and residual values for friction angle of 35° and 30 and heights for 0.008 m and 0.005 m mesh size models.

Soil arch height (m)		
	Parabolic	**Triangular**
Peak	0.018	0.036
Residual	0.022	0.044
0.01 m	0.014	0.034
0.008 m	-	0.044
0.005 m	-	0.041

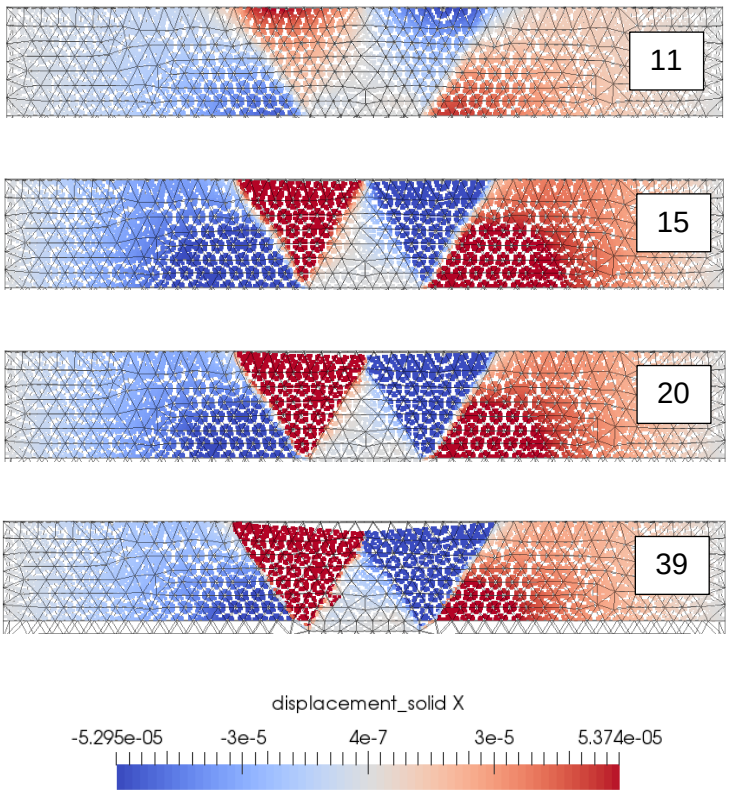

Figure 5.12 Horizontal Displacement Evolution for 0.008 m mesh size. Time step is shown in each plot.

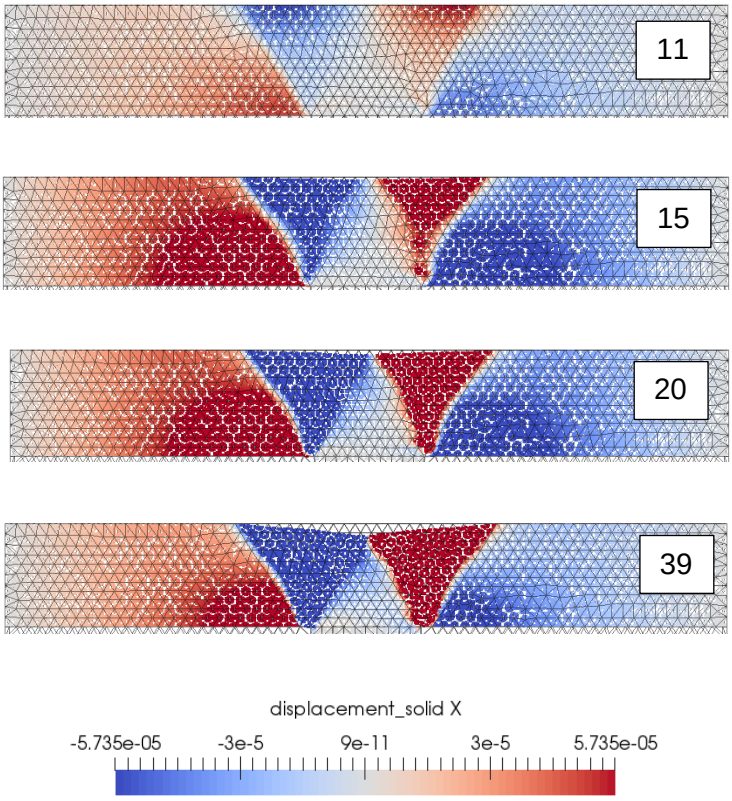

Figure 5.13 Horizontal Displacement Evolution for 0.005 m mesh size. Time step is shown in each plot.

5.4. Peak and Residual Friction Angle

Figure 5.14 shows that loading behaviour for the three models is similar. For friction angles, the load stabilizes at lower values. Effective vertical stress on the trapdoor presents similar distribution for the three cases (Figure 5.15).

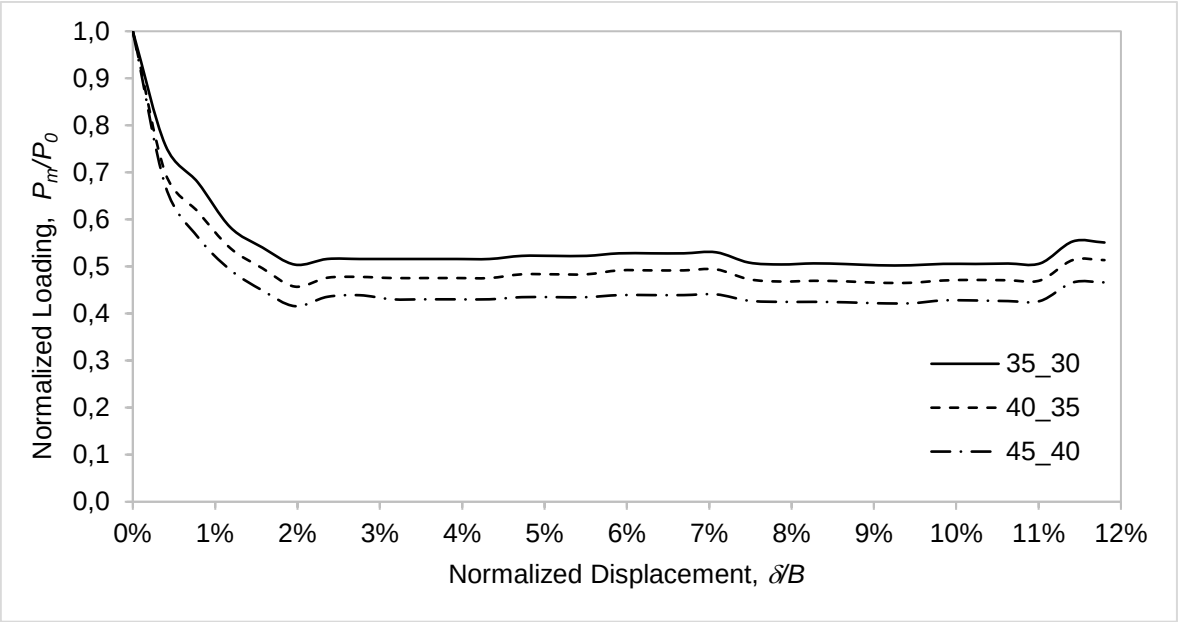

Figure 5.14. Normalized Loading P_m/P_0 versus Normalized Displacement δ/B for mesh sizes for base model and F1 (ϕ_p=40, ϕ_r=35) and F2 (ϕ_p=45, ϕ_r=40) models.

Figure 5.15 Effective Vertical Stress σ'_y for minimum load time step versus Relative Distance to Trapdoor Left Edge n for base model and F1 (ϕ_p=40, ϕ_r=35) and F2 (ϕ_p=45, ϕ_r=40) models.

For model F1, break point and minimum load normalized loads are 0.539 and 0.465, and for model F2, 0.493 and 0.422 respectively, lower than those of base model (Table 5.8). According to theorical values (Table 5.9 and 5.10) minimum load for models F1 and F2 fall between triangular and intermediate terminal state arch. Despite the higher strength for models F1 and F2, neither of them presented parabolic or triangular arch mechanism, unlike

base model. One reason may be related to mesh geometry, which was the same for the three cases.

Table 5.8 Normalized loading of pivotal states for 0.01 m, 0.008 m and 0.005m mesh sizes.

	Break Point		Minimum Load		End of the Test	
$\phi_p\_\phi_r$	P_m/P_0	δ/B (%)	P_m/P_0	δ/B (%)	P_m/P_0	δ/B (%)
35_30	0.584	1.2%	0.503	9.1%	0.551	11.8%
40_35	0.539	1.2%	0.465	9.4%	0.514	11.8%
45_40	0.493	1.2%	0.422	9.4%	0.466	11.8%

Table 5.9 Minimum normalized loading P_m/P_0 estimation according to Iglesia et al (2014) proposed formulas for soil arching, considering peak and residual values for friction angle of 40° and 35° and H/B=1.

H/B=1	K_E	P_m/P_0 parabola	P_m/P_0 triangular	P_m/P_0 intermediate
Peak	0.415	0.352	0.384	0.594
Residual	0.505	0.394	0.445	0.570

Table 5.10 Minimum normalized loading P_m/P_0 estimation according to Iglesia et al (2014) proposed formulas for soil arching, considering peak and residual values for friction angle of 45° and 40° for H/B=1.

H/B=1	K_E	P_m/P_0 parabola	P_m/P_0 triangular	P_m/P_0 intermediate
Peak	0.333	0.314	0.332	0.515
Residual	0.415	0.352	0.384	0.495

Figures 5.16 and 5.17 show deviatoric strain evolution and Figures 5.18 and 5.19 horizontal displacement evolution. The plots present similar behaviour for both models, where two slip surfaces reach the surface around time step 13 and a triangle shape is formed above the trapdoor. The deformation of soil corresponds with a intermediate terminal state. The height of the triangle was measured and compared with theorical values (Table 5.11) and for both models it was close to triangular height of 40°.

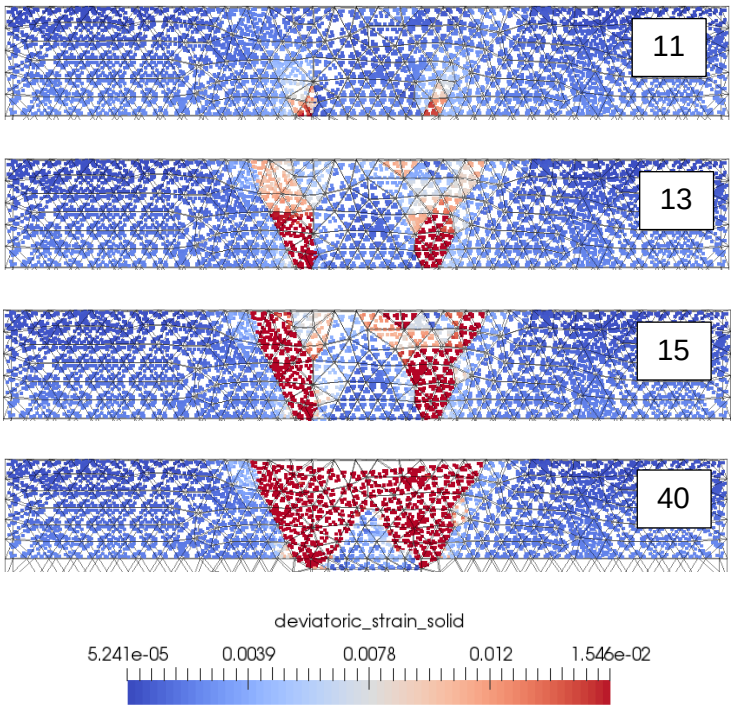

Figure 5.16 Deviatoric Strain Evolution for model F1 (ϕ_p=40, ϕ_r=35) and *H/B*=1. Time step is shown in each plot.

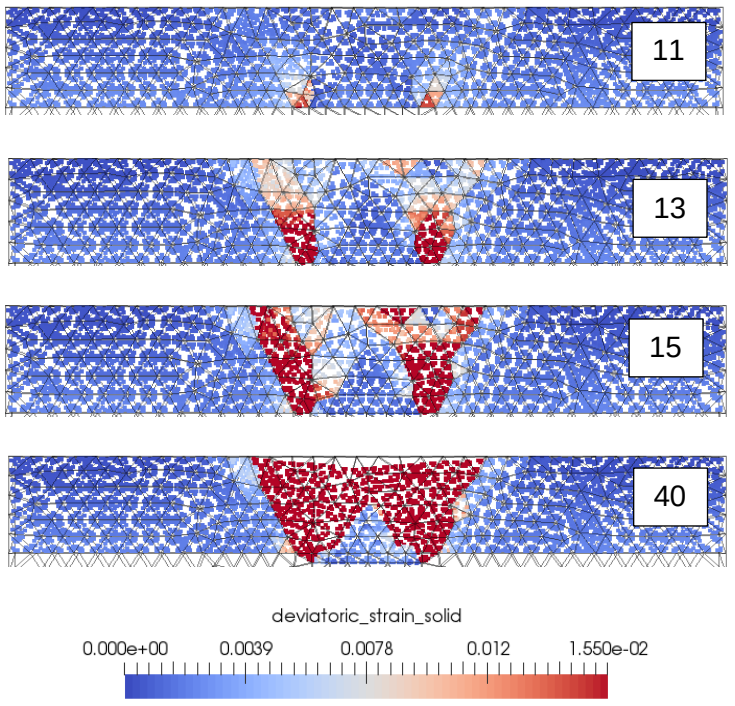

Figure 5.17 Deviatoric Strain Evolution for model F2 (ϕ_p=45, ϕ_r=40) and *H/B*=1. Time step is shown in each plot.

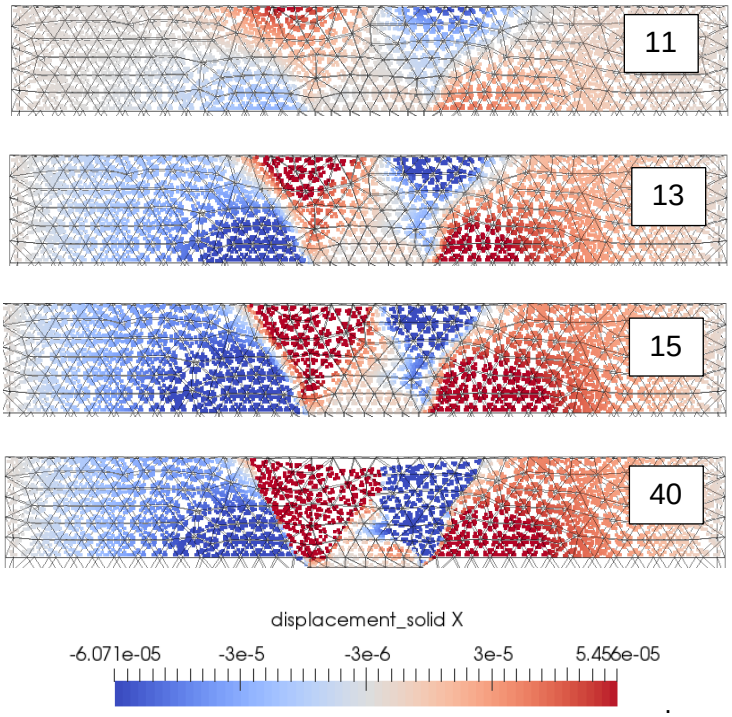

Figure 5.18 Horizontal Displacement Evolution for model F1 (ϕ_p=40, ϕ_r=35) and *H/B*=1. Time step is shown in each plot

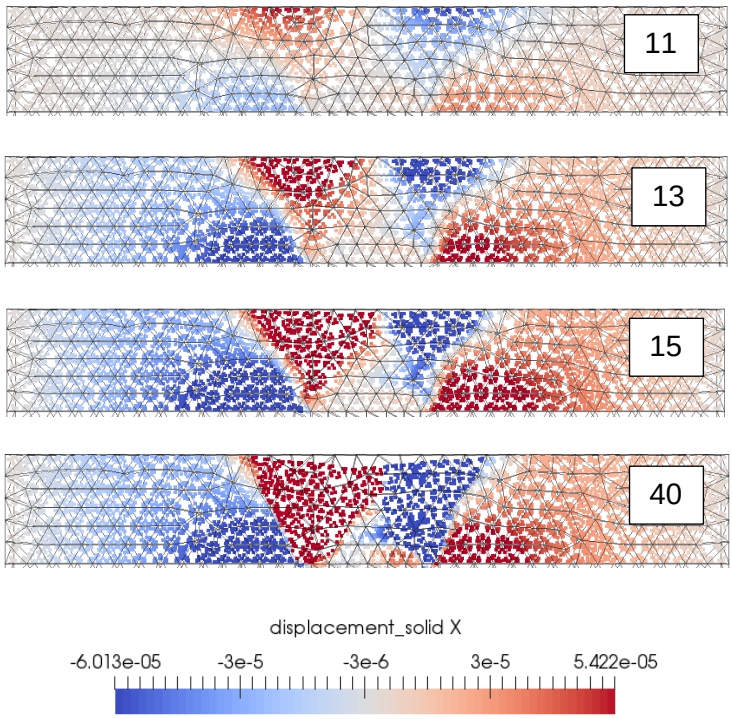

Figure 5.19 Horizontal Displacement Evolution for model F2 (ϕ_p=45, ϕ_r=40) and *H/B*=1. Time step is shown in each plot.

Table 5.11 Soil arch height for parabolic and triangular shapes according to Iglesia et al (2014) considering friction angles of 35°, 40° and 45° for *H/B*=1.

	Soil arch height (m)	
	Parabolic	**Triangular**
35°	0.018	0.036
40°	0.015	0.030
45°	0.013	0.025
40_35 m	-	0.032
45_40 m	-	0.030

6. A Simplified Approach of Sinkhole Developments in Unsaturated Soils

Taking as reference the results of Wang et al (2016) sensitivity study of active and passive arching, and the material point method for unsaturated soils presented by Yerro et al (2015), MPM code was used to study the response of a stable dry soil layer over a cavity subjected to cohesion loss. This model represents a simplified approach to study sinkhole development in an unsaturated triggered by water inflow.

6.1. Introduction

6.1.1. Sensitivity Study of Active and Passive Arching

Wang et al (2016) carried out an investigation on active and passive arching stresses in frictional soils with cohesion and their approach included a sensitivity study using upper and lower bound limit analysis. The first one was performed with Discontinuity Layout Optimization (DLO) algorithm, which employs optimization techniques to find one or a set of critical yield surfaces, whereas the second one was performed in a finite element software with and adaptive mesh algorithm. The material modelled was a homogeneous isotropic soil with shear strength represented by Mohr-Coulomb failure criterion. A scheme of the model is shown in Figure 6.1 where boundary conditions are specified for each bound limit analysis. Figure 6.2 presents the adaptive mesh refinement and the discontinuity layout optimization of slip planes for lower and upper bound analysis respectively.

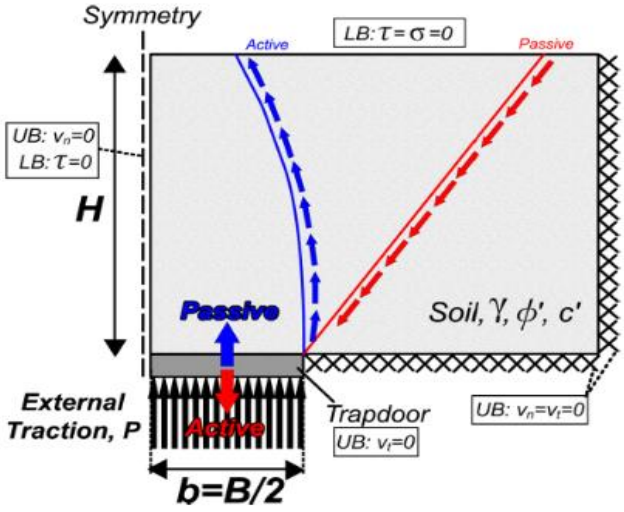

Figure 6.1 Scheme of trapdoor model. (Wang et al, 2016)

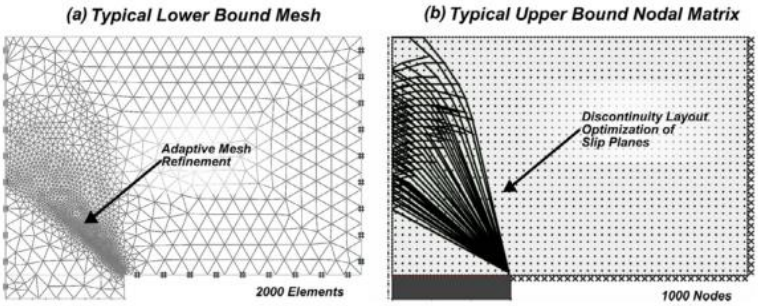

Figure 6.2 Adaptive mesh refinement and discontinuity layout optimization of slip planes for lower and upper bound analysis. (Wang et al, 2016)

Two loads were applied below the trapdoor to calculate the collapse load, an upward stress P_0 equivalent to geostatic value (γH) and downward increasing stress ΔP. When collapse took place, the active arching load P was obtained as the difference between P_0 and ΔP and then normalized as a P/P_0 ratio. With this analysis, only terminal state collapse loads were estimated. Investigation results presented good agreement between lower and upper bound analysis. Also, they were compared with previous studies and were bracketed by Engesser (1882) and Ladanyi and Hoyaux (1969) formulas.

Charts were elaborated as a result of the analysis. Cohesion values are presented as a normalized stability number N_s which is defined as $c/\gamma H$. Figure 6.3 shows upper bound charts for friction angles of 20°, 25°, 30° and 35°. As H/B increases, active load ratio decreases and the failure mechanism associated also changes, as reported on Figure 6.4.

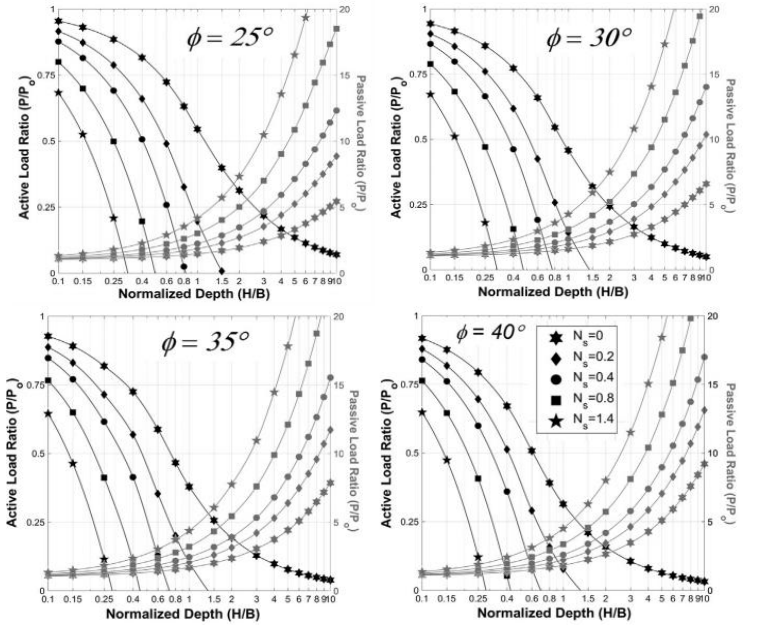

Figure 6.3 Upper Bound Limit Analysis for active and passive load ratios for different normalized depths, internal angles of friction and normalized stability numbers. (Wang et al, 2016)

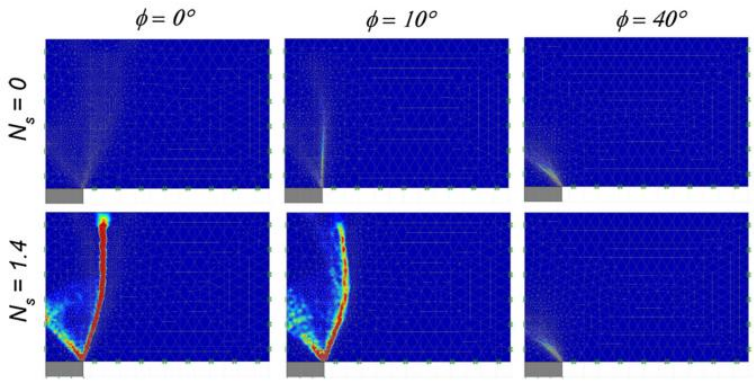

Figure 6.4 Collapse mechanisms for *H/B*=2 for lower bound analysis. (Wang et al, 2016).

The influence of cohesion increase on active load ratio is significantly important. For example, for a friction angle of 40° with zero cohesion and *H/B*=1, active load ratio is close to 0.1 but increasing N_s to 0.4 would yield a negative ratio, meaning that soil is pulled down in order to collapse. According to Wang et al (2016) this value is representative of no arching load or a stable subsurface void. This effect was further studied by determining a H/B_{crit} for a zero or negative P/P_0 value for different friction angles, as Figure 6.5 shows. For instance, for a friction angle of 10° and N_s increased from 0.2 to 1.4, H/B_{crit} shifts from 2.5 to 0.35 and consequently, trapdoor length would increase in 614% before collapse. Nonetheless, the authors note that trapdoor arching is not a stable condition and could be affected by movement or saturation.

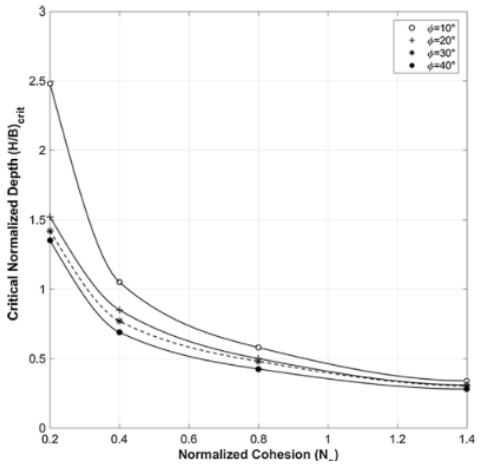

Figure 6.5 H/B_{crit} for active trapdoor and cohesion values. (Wang et al, 2016).

One particular conclusion drawn from these results is that a cohesionless soil with an angle of friction between 10° to 40° would not be stable without support. Deep trapdoor (*H/B*>1.5 or 2) equilibrium would be sustained with at least a little more than a N_s of 0.2. Figure 6.6 shows active load ratios for a friction angle of 10°.

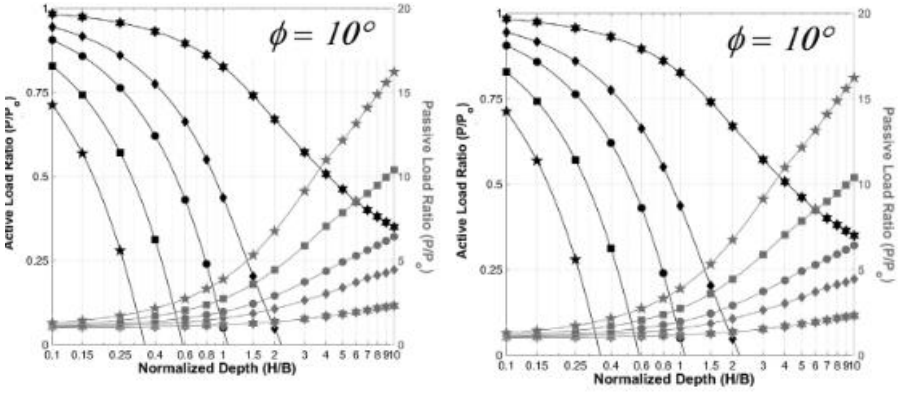

Figure 6.6. Upper Bound and Lower Bound Limit Analysis for active and passive load ratios for a friction angle of 10° (Wang et al, 2016).

6.1.2. MPM Code for Unsaturated Soil

Large deformations can be triggered in unsaturated soil. In order to analyze this behaviour, Yerro et al (2015) developed a code for unsaturated soils using a three-phase single-point MPM formulation of coupled flow and studied a case inspired in road embankments damages as a consequence of heavy rainfalls. Slides of up to 4 meters were reported after the event.

According to Yerro et al (2015), instability of unsaturated slopes is essentially governed by the evolution of apparent soil cohesion and friction angle with evolving suction; and in general, both cohesion and friction depend non-linearly on suction. The mechanical constitutive model used was defined by a Mohr-Coulomb expression:

$$\tau = c + \bar{\boldsymbol{\sigma}}_n \tan\varphi \qquad \text{(Eq 6.1)}$$

Where $\bar{\boldsymbol{\sigma}}_n$ represents the constitutive normal stress to a reference plane. Strength parameters are defined following

$$c = c' + c_s \qquad \text{(Eq 6.2)}$$
$$\varphi = \varphi' + \varphi_s \qquad \text{(Eq 6.3)}$$

Where c' and φ' represent effective cohesion and effective friction for saturated conditions. The effect of suction in material strength is included in the second parameter, as follows,

$$c_s = \Delta c_{max}\left[1 - e^{-B(s/P_{atm})}\right] \qquad \text{(Eq 6.4)}$$

And

$$\varphi_s = A(s/P_{atm})$$

Where P_{atm} is the atmospheric pressure, B controls the rate of variation of apparent cohesion with suction and A controls friction angle dependence with suction. Table 6.1 presents the parameters used in their study. For a maximum change of suction of 800 kPa, friction variation was less than 1° and cohesion shifted from 67 kPa to 1 kPa for saturated conditions.

Table 6.1 Constitutive model parameters used in Yerro et al (2015).

Parameter	Value
Young Modulus (MPa)	10
Cohesion, c' (kPa)	1
Friction Angle, ϕ' (°)	20
Δc_{max} (kPa)	15
A	0.07
B	0.01

In their study, wetting induced by rainfall on the embankment slope is modelled by means of suction decrease on ground surface from 800 to 0 kPa during 10 s. The saturated condition is maintained afterwards to the end of the simulation, which generates a downward flow due to suction gradients. Figure 6.7 presents suction and equivalent shear strain contours at five different times. Slope instability is triggered at 35 s, when substantial reduction in suction has taken place.

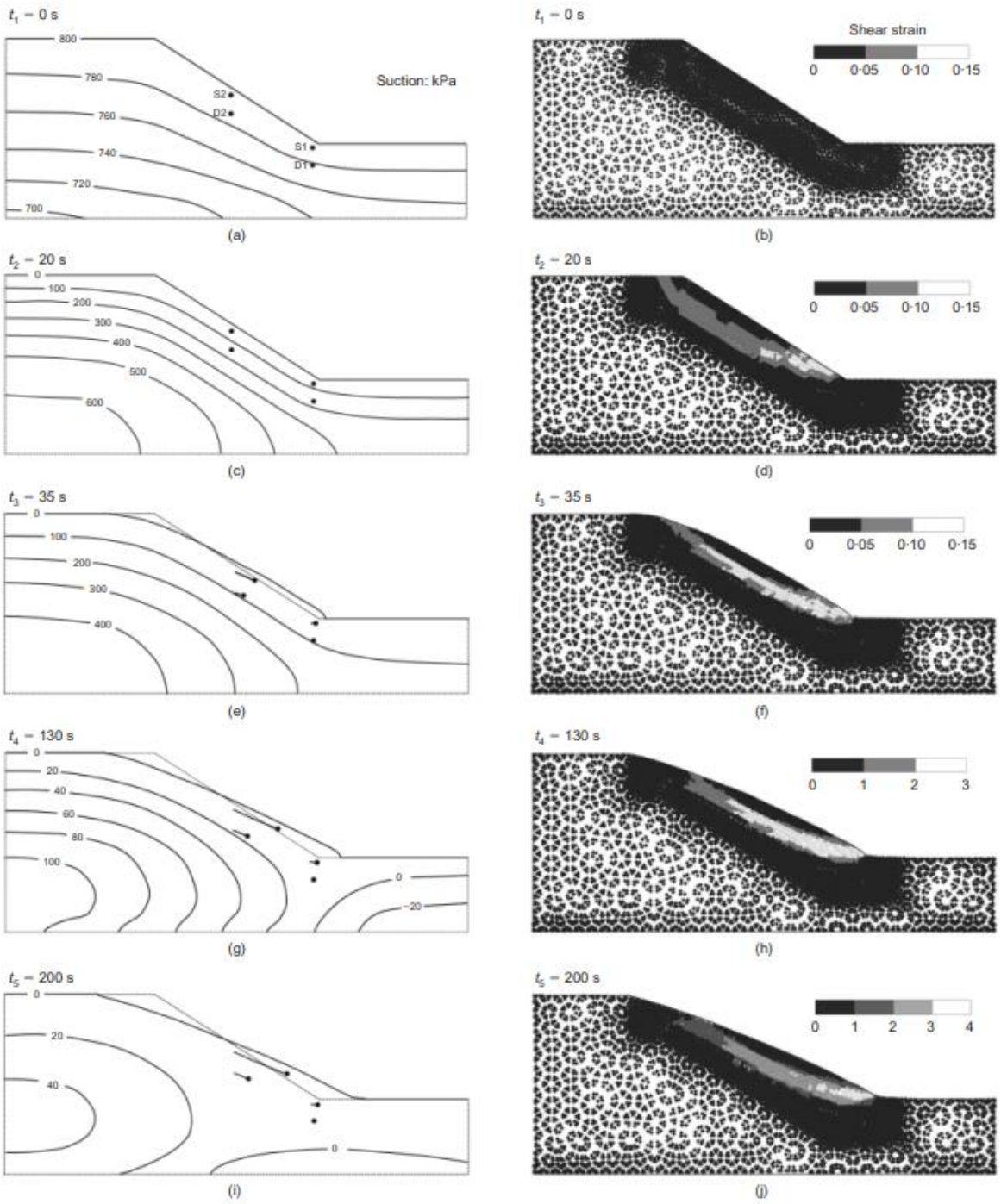

Figure 6.7 Calculated suction and equivalent shear strain contours at three different times. (Yerro et al, 2015)

6.2. Sinkhole Model description

In the light of Wang et al (2016) and Yerro et al (2015) publications, a model with MPM code was developed as a simplified approach to study sinkhole developments in unsaturated soil. The following considerations were taken in account:

- Dry soil modelled with strain softening Mohr-Coulomb constitutive model.
- Deep trapdoor (cavity) condition, *H/B*=4.
- Direct reduction of peak cohesion value as a means of simulating water inflow and suction decrease. Two patterns of flux were analyzed.
- A void zone that represents a cavity in a karstic substratum.

6.2.1. Geometry

A scheme of the sinkhole model is showed in Figure 6.8, which consists of three layers of soil with the same depth and a void zone below it. The values for each parameter are presented in Table 6.2.

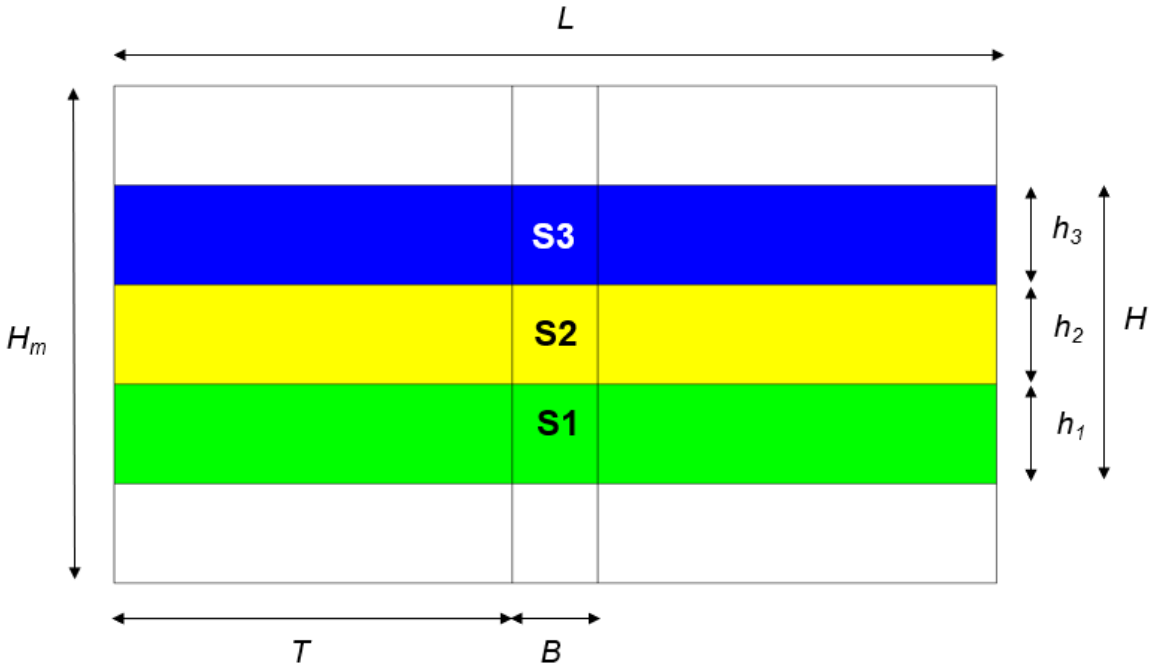

Figure 6.8 Scheme for sinkhole model.

Table 6.2 Sinkhole model geometry parameters.

Description	Symbol	Unit	Value
Model height	H_m	m	5
Model thickness	*w*	m	0.1
Model lenght	*L*	m	7.75
Soil total depth	*H*	m	5
Soil layer *S1* depth	h_1	m	1
Soil layer *S2* depth	h_2	m	1
Soil layer *S3* depth	h_3	m	1
Trapdoor lenght	*B*	m	0.75
Distance to cavity edge	*T*	m	3.5

6.2.2. Boundary Conditions

The model presents x-fixities at both lateral sides and total fixity at the bottom. Soil layer bottom has y-fixity.

To trigger sinkhole development, y-fixity at the center of soil is removed.

6.2.3. Materials

Soil behaviour was modelled with strain softening Mohr-Coulomb constitutive law presented by Yerro et al (2014).

Table 6.3 Base model material parameters.

Material Paramaters	Unit	Soil
Material Type		1 ph. Solid
Porosity Solid		0.35
Density Solid	kg/m^3	2700
K0 Value Solid		0
Intrinsic Permeability Solid	m^2	0
Material Model Solid		SS MC
Young Modulus	kPa	5000
Poisson Ratio		0.35
Peak Cohesion	kPa	10
Residual Cohesion	kPa	0.1
Peak Friction Angle	°	35
Residual Friction Angle	°	30
Peak Dilantancy Angle	°	0
Residual Dilantancy Angle	°	0
Shape Factor η		500

The selected initial peak value was compared with Wang et al (2016) stability charts. As mentioned before, a N_s of at least 0.2 is required to sustain stability without support for deep trapdoors in soils with friction angles between 10° to 40°. For this model, geostatic stress is 51.7 kPa and the theorical value for peak cohesion was estimated in 10.3 kPa. Given that *H/B*=4, 10 kPa was considered sufficient to grant stability.

Classic Mohr-Coulomb constitutive law formulation was not applied for modelling soil behaviour because it lead to calculation errors, such as not allowing material points to reach the bottom of the void zone.

6.2.4. Loading conditions

Quasistatic equilibrium is applied to calculate initial stresses in the soil in 5 time steps of 5 s each. Once the y-fixity is removed, only gravity loads are applied.

6.2.5. Mesh

An unstructured mesh of 0.1-m long tetrahedral elements was used for the model. Also, 4 material points were assigned to each element. Figure 6.9 shows the mesh and material point distribution used in the simulation.

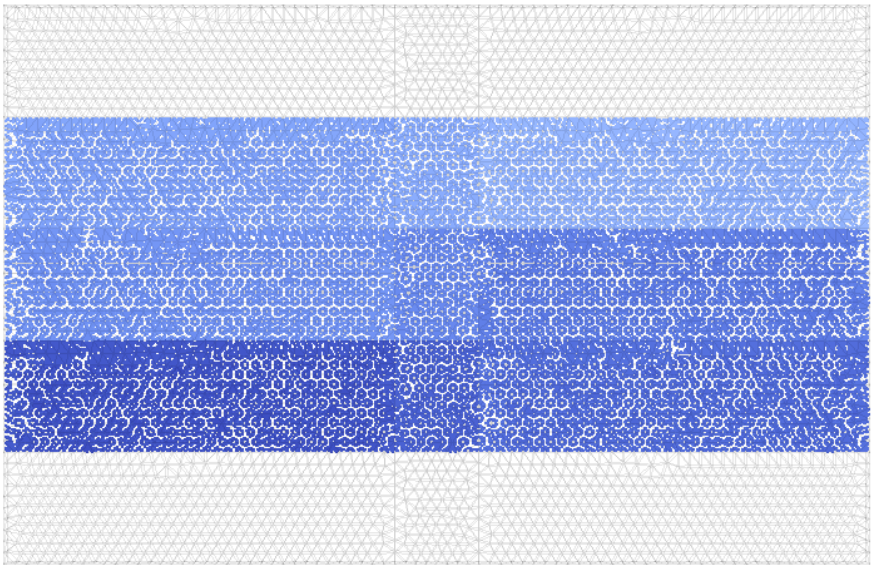

Figure 6.9 Mesh and material point distribution for sinkhole model.

6.2.6. Numerical Parameters

For the quasistatic and dynamic stages, damping factors of 0.75 and 0.05 are used respectively.

6.2.7. Simulation of Water Inflow

Ten time steps of 0.1 s were applied after the release of the y-fixity. Then, two patterns of cohesion loss were applied as a means of simulating upward and downward water flow.

Upward flow

Cohesion loss was applied considering a 25% reduction of peak value c_p every 10 time steps, initially affecting the deepest soil layer *S1* and later the two remaining layers. For instance, at time step 25 c_p reduction is applied for the first time in *S2* whereas *S1* peak value is decreased in 50%. Table 6.4 presents the complete pattern for upward flow simulation.

Table 6.4 Peak cohesion c_p loss pattern for simulating upwards flow.

Peak cohesion c_p (kPa)			
Time step	**S1**	**S2**	**S3**
6	10	10	10
16	7.5	10	10
26	5.0	7.5	10
36	2.5	5.0	7.5

Downward flow

Downward flow is simulated in a similar fashion as upward flow. Table 6.5 presents the complete pattern for downward flow simulation.

Table 6.5 Peak cohesion loss c_p pattern for simulating downward flow.

Peak cohesion c_p (kPa)			
Time step	**S1**	**S2**	**S3**
6	10	10	10
16	10	10	7.5
26	10	7.5	5.0
36	7.5	5.0	2.5
46	5.0	2.5	0.1
56	2.5	0.1	0.1

6.3. Sinkhole Model Quasistatic Results

Figure 6.10 and 6.11 show the initial effective vertical and horizontal stress.

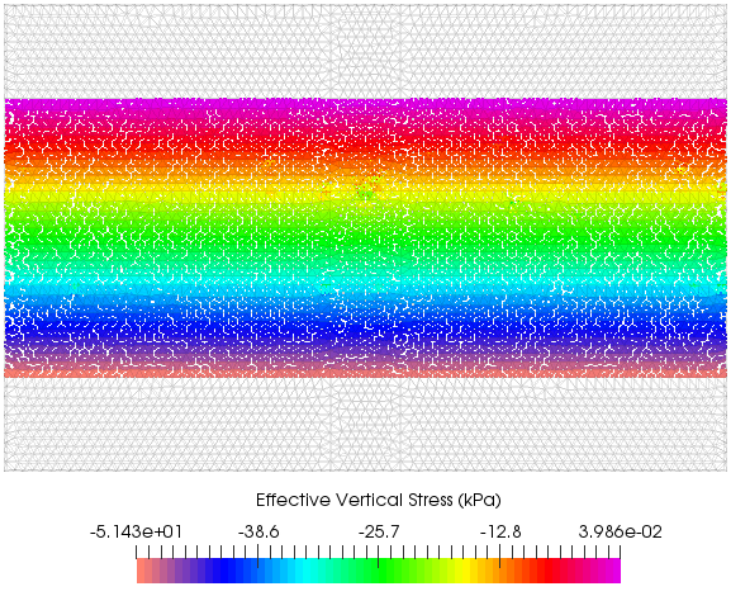

Figure 6.10 Initial Effective Vertical Stress for sinkhole model.

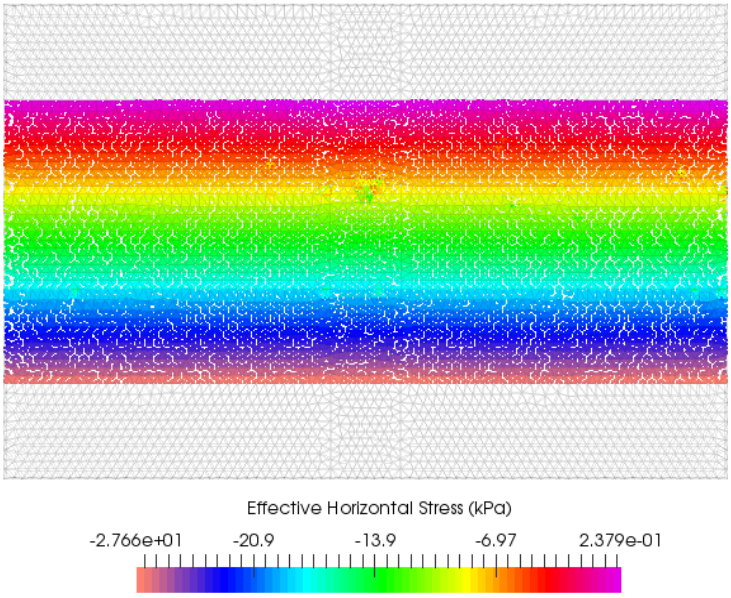

Figure 6.11 Initial effective Horizontal Stress for sinkhole model.

6.4. Sinkhole model Dynamic Results

The reduction of cohesion peak values was applied until the particles located above the void zone started to displace reaching the bottom of the model. Deviatoric strains were analyzed to study the development of slip surfaces throughout the simulation.

6.4.1. Upward Flow

At time step 15, a triangular-shaped slip surface is formed above the portion of soil placed over the cavity. Deviatoric strain is constant until time step 36, when the sinkhole is triggered. At this moment, the values of c_p have been decreased down to 2.5, 5 and 7.5 kPa in layers *S1*, *S2* and *S3* respectively and the average of the three soil layers is 5 kPa which corresponds to a stability number N_s of 0.097. Additional slip surfaces develop from the bottom layer and reach the surface. The affected superficial areas also present some slip surface that deepen towards the middle soil layer.

At time step 45, large displacements have taken place. Soil particles partially fill the void zone, which represents a cavity in karstic substratum, and the sinkhole has started to form in the surface. A group slip surfaces are found at the sides of the sinkhole.

At final time step 56, the soil particles within the void zone have been uncapable of further displacement and the group rest at an angle of 75° with the horizontal plane, 2.5 times higher than the residual friction angle, which suggests that soil has not still reached equilibrium conditions. The sinkhole spreads up to 5.8 m and the value of the deepest settlement in the center is 0.4 m. The slip surfaces that stem from the top of the void zone make an angle of

58° with the horizontal plane which is close to Rankine's angle for an active rupture surface ($45° + \frac{\varphi}{2} = 60$, for residual friction angle).

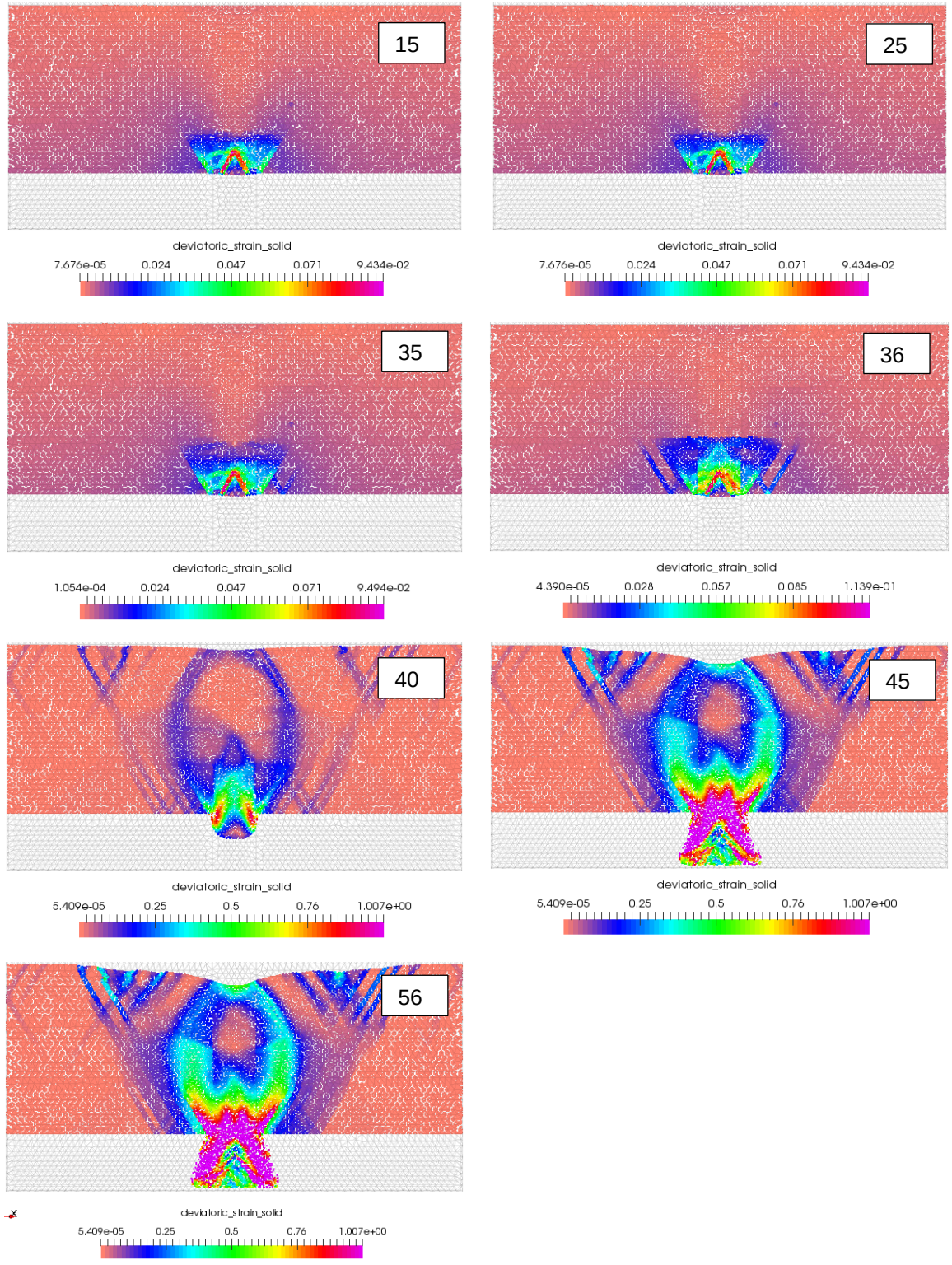

Figure 6.12 Deviatoric Strain distribution for upward flow. Time step is shown in each plot.

6.4.2. Downward flow

Figure 6.13 presents the deviatoric strain evolution for downward flow simulation.

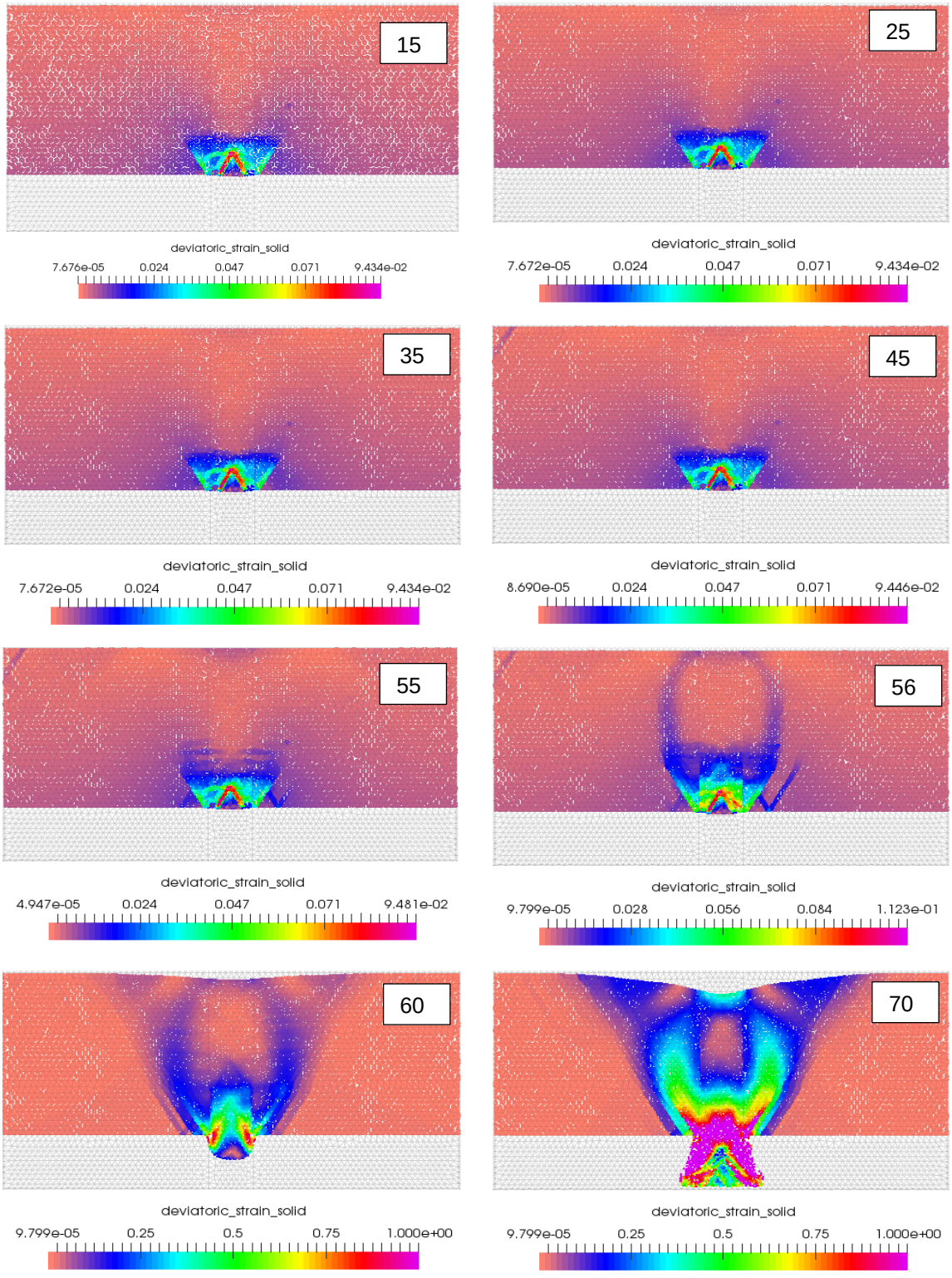

Figure 6.13 Deviatoric Strain distribution for downward flow. Time step is shown in each plot.

Downward flow case required more time steps to trigger the sinkhole. At time step 15, a triangular-shaped slip surface is formed above the portion of soil placed over the cavity. Deviatoric strain is approximately constant until time step 56, when the sinkhole is triggered. At this moment, the values of c_p have been decreased down to 0.1, 0.1 and 2.5 kPa in layers S1, S2 and S3 respectively and the average of the three soil layers is 0.9 kPa which corresponds to a stability number Ns of 0.02, only 20% of upward flow value. In contrast with upward flow, only two thin slip surfaces reach the surface and only one local additional slip surface has developed from the bottom layer.

At time step 60, large displacements have taken place and sinkhole formation has been triggered. The sides of the sinkhole have developed triangular-shaped deformed zones of soil.

At final time step 70, the soil particles within the void zone have been uncapable of further displacement and the group rest at an angle of 70° with the horizontal plane, 2 times higher than the residual friction angle, which suggests that soil has not still reached equilibrium conditions as in upward flow case.

The sinkhole spreads up to 5.6 m and the value of the deepest settlement in the center is 0.4 m. The triangle-shaped deformed zone at the border of the sinkhole has widened and presents a smooth curve of settlements, in contrast with upward flow case where a set of slip surfaces were formed instead and settlements were more irregular. One reason for such configuration may be the amount of strength loss, in the first case cp of the top layer was only decreased in 25% whereas for the second case, c_p was reduced to 0.1 kPa.

The slip surfaces that stem from the top of the void zone make an angle of 59° with the horizontal plane which is close to Rankine's angle for an active rupture surface ($45° + \frac{\varphi}{2} = 60$, for residual friction angle).

7. Conclusions

This present work consists of an approach to study sinkhole development over karstic substratum with Material Point Method (MPM). In this section, main conclusions are presented.

Trapdoor experiment modelling

The classical yielding trapdoor experiment was modelled taking as reference Iglesia et al (2011) experiments on a geotechnical centrifuge. The results show that MPM is capable of simulating the experiment and the soil overall behaviour, as seen in the normalized loadings versus normalized displacement plots. Break point displacement value was close to the average; however, minimum load displacement did not fall between the average range reported. Minimum load fell between parabolic and triangular shape arch, as expected for shallow conditions. Deviatoric strain plots showed the formation of a triangular arch at intermediate trapdoor displacements, but also external slip surfaces that correspond with terminal state deformation at large displacements. Nonetheless, it was possible to identify parabolic arch at horizontal displacement plots. Horizontal stresses in the vicinity of the trapdoor showed an increase with trapdoor displacement, as expected for stress redistribution. Break point was found to have influence in horizontal stresses in the same fashion as in vertical stresses.

Parametric study of trapdoor modelling

The parametric study presented some difficulties for MPM modelling, probably of mesh dependency.

Normalized depth variation showed that MPM was still capable of modelling overall loading behaviour, as higher *H/B* ratios reported smaller normalized loadings as expected but was unable to model the arch mechanism accurately since results showed that minimum load for such ratios fell between triangular and intermediate state arching. Such findings are compatible with deviatoric strain plots, where it is clear that typical terminal state slip surfaces develop first than triangular arching. In spite of these results, parabolic arch was identified in horizontal displacement plots. Break points displacements were close to the average, though minimum load still reported larger displacements than the average range.

Mesh element size variation presented the same issues as normalized depth. Minimum load substantially increased with refinement, approaching more to intermediate terminal state theorical value. This is compatible with deviatoric strain plots, where external slip surfaces develop from the beginning and even in horizontal displacement plots, only triangular arching is identified.

Friction angle variation loading behaviour reported overall smaller values than base model, since the angles were higher than base model. However, minimum loads were close to intermediate terminal state theorical values. Break point as well as minimum load

displacement were the same for the three cases. Deviatoric strain plots were practically the same as base model and parabolic arch could not be identified in horizontal displacement plots.

A simplified approach of sinkhole developments in unsaturated soils

Regarding the simplified approach is clear that, in light of trapdoor experiment results, mesh dependency affects the real solution. Nonetheless, this approach serves as a starting point to further research on this topic.

Water inflow condition is a key factor on the sinkhole triggering and needs to be properly analyzed. For instance, results show that downward inflow requires more time (more strength loss) to trigger the sinkhole. However, the cohesion loss pattern as proposed here is a really basic approach to real rainfall or water table decline effect, and this approach is proposed for a dry soil layer. A more sophisticated code, such as MPM for unsaturated soils, would be capable of dealing with such limitations.

One of the main characteristics of karstic substratum is the presence of cavities, due to dissolution of rock. In this approach, a cavity of 7.75 m length and 1 m depth was modelled, but a parametric study would elucidate the effect of larger void zones. Also, further attention is required in particle motion in this zone, since final equilibrium could not be reached in spite of adding more time steps to the calculation and the resting angle of the group of particles in this zone was higher than residual friction angle.

8. References

Abdulla, W. and Goodings, D. 1996. Modelling of sinkholes in weakly cemented sand. Journal of Geotechnical Engineering 122(12): 998-1005.

Adachi, T., Kimura, M., Nishimura, T., Koya, N., and K. 1997. Trap door experimental under centrifugal conditions. Deformation and progressive failure in geomechanics. A. Asaoka, T. Adachi, and F. Oka, eds., Pergamon, New York, 725 – 730.

Al-Kafaji, I.K.J. 2013. Formulation of a Dynamic material point method (MPM) for geomechanical problems.

Augarde, C. and Lyamin, A. and Sloan, S. 2003. Prediction of Undrained Sinkhole Collapse. Journal of Geotechnical Geoenvironmental Engineering. 129(3):197-205.

Chevalier, B. COmbe, G., and Villard, P. 2009. Experimental and numerical study of the response of granular layer in the trap-door problem. Powder and Grains 2009. Proceedings, 6th International Conference on the Micromechanics of Granular Media. M. Nakagawaand S Luding eds. American Institute of Physic, Melville, NY, 649-652.

Costa, Y. D., Zornberg, J.G., Bueno, B.S., and Costa, C.L. 2009. Failure mechanisms in sand over a Deep active trapdoor. Journal Geotechnical and Geoenvironmental Engineering. 10.1061/(ASCE)GT.1943-5606.0000134, 1741-1753.

Cummis, S.J. and Brackbill, J.U. 2002. An implicit particle-in-cell method for granular materials. Journal of Computational Physics.

Dewoolkar, M.M., Santichaianant, K., and Ko, H.-Y. 2007. Centrifuge modelling of granular soil response over active circular trapdoors. Soils and Foundations 47(5),931-945.

Engesser, Fr. 1882. Ueber den Erdduck gegen innere Stüzwande (Tunnelwande). Deutsche Bauzeitung, 16, 91-93 (in German).

Evans, C.H. 1983. An examination of arching in granular soils. S. M. Thesis, Department of Civil Engineering, MIT, Cambridge, MA.

Gutiérrez, F., Cooper, A.H., Johnson, K.S. 2007. Environmental Geology. DOI10.1007/s00254-007-07028-4.

Gutiérrez, F., Guerrero, J. and Lucha, P. 2007. A genetic classification of sinkholes illustrated from evaporite paleokarst exposures in Spain. Environmental Geology. 53:993-1006.

Gutiérrez, F., Guerrero, J. and Lucha, P. 2008. Quantitative Hazard assessment. A case study from Ebro Valley evaporite alluvial karst (NE Spain). Natural Hazards 45:211-233.

Harlow, F.H. 1964. The particle-in-cell computing method for fluid dynamics. Methods in Computational Physics, 3(3):319-343.

Iglesia, G.R., Einstein and H.H., Whitman, R.V. 2013. Investigation of soil arching with centrifuge tests. Journal of Geotechnical and Geoenvironmental Engineering.140(2):04013005.

Iglesia, G.R., Einstein and H.H. Whitman, R.V. 2011. Validation of centrifuge model scaling for soil systems via trapdoor tests. Journal of Geotechnical and Geoenvironmental Engineering. Eng. 10.1061/(ASCE)GT.1943-5606.0000517, 10-1089.

Krynine, D.P. 1945. Discussion of “Stability and stiffness of cellular cofferdams” by Karl Terzaghi. Transactions of the American Society of Civil Engineers. 110, 1175-1178.

Ladanyi, B. and Hoyaux, B. 1969. A study of the trapdoor problem in a granular mass. Canadian Geotechnical Journal 6(1), 1 – 15.

Linker, R. and Klar, A. 2017. Detection of sinkhole formation by strain profile measurements using BOTDR: simulation study. Journal of Engineering Mechanics. 143(3): B4015002.

Lysmer, J., and Kuhlemeyer, L., 1969. Finite dynamic model for infinite media. Journal of the Engineering Mechanics Division, 3:859-977.

Stone, K.J.L. 1988. Modelling of rupture development in soils. Ph.D. dissertation, Wolfson College, Cambridge University, Cambridge, U.K.

Sulsky, D., Chen, Z. and Schreyer, H.L. 1994. A particle method for history-dependent materials. Computer Methods in Applied Mechanics and Engineering, 118(1-2):179-196.

Sulsky, D., Zhou, S. and Schreyer, H.L. 1995. Application of particle-in-cell method to solid mechanics. Computer Physics Communications, 87(1-2):236-252. ISSN 0014655.

Sulsky, D., and Schreyer, H. 1996. Axysymmetric form of the material point method with application to upsetting and Taylor impact problems. Computer Methods in Applied Mechanics and Engineering. 0457825(96).

Terzaghi, K. 1936. Stress distribution in dry and saturated sand above a yielding trapdoor. Proceedings 1st Conference on Soil Mechanics and Foundations Engineering, Graduate School of Engineering. Harvard University, Cambridge, MA, 307-311.

Tharp, T. 1999. Mechanics of upward propagation of cover-collapse sinkholes. Engineering Geology 52 (1999) 23-33.

Vardoulakis, I., Graf., B and Gugehus, G. 1981. Trap-door problem with dry sand: A statical approach based upon model test kinematics. International Journal for Numerical and Analytical Methods in Geomechanics. 5(1), 57-58.

Waltham, T. 2009. Sinkhole geohazards. Geology Today, Vol. 25, No.3 May-June.

Waltham, T. 2008. Sinkhole hazard case histories in karst terrains. Quarterly Journal of Engineering Geology and Hydrogeology, 41, 291-300.

Waltham, T. 2011. Fengcong, fenglin, cone karst and tower karst. 2011. Cave and Karst Science, 35(3), 77-88.

Wang, L., Leshchinsky, B., Evans, T. and Xie, Y. 2016. Active passive arching stresses in c'-ϕ' soils: A sensitivity study using computational limit analysis.

Yerro, A. 2015. MPM modelling of landslides in brittle and unsaturated soils. Phd Thesis. Universitat Politècnica de Catalunya.

Youssef, A., Al-Harbi, H. Gutiérrez, F., Zabramwi, Y., Bulkhi, A., Zahrani, S., Bahamil, A., Zahrani, A., Otaibi, Z. and El-Haddad, B. 2016. Natural and human-induced sinkhole hazards in Saudi Arabia: distribution, investigation, causes and impacts. Hydrogeol Journal. 24:625-644.

Zienkiewicz, O.C., Taylor R.L. and Zhu, J. Z. 1967. The Finite Element method. S.1.: McGraw-Hill, 1967. ISBN 0 7506 6320 0.